Chemical and Biological Sensors Based on Organic Semiconductors

by

Mihail Bora

Submitted to the Department of Physics
in partial fulfillment of the requirements for the degree of

Doctor of Philosophy in Physics

at the

MASSACHUSETTS INSTITUTE OF TECHNOLOGY
[June]
March 2009

Author ....
Department of Physics
March 13, 2009

Certified by..
Marc A. Baldo
Associate Professor
Thesis Supervisor

Certified by..
Alexander van Oudenaarden
Professor
Thesis Supervisor

Accepted by ....
Thomas Greytak
Chairman, Associate Department Head for Education

Chemical and Biological Sensors Based on Organic Semiconductors

by

Mihail Bora

Submitted to the Department of Physics
on March 13, 2009, in partial fulfillment of the
requirements for the degree of
Doctor of Philosophy in Physics

Abstract

In this thesis I designed, fabricated and characterized two types of sensors: chemical sensors based on organic thin film transistors, and a miniaturized surface plasmon resonance biosensors for biotechnology and medical diagnostics applications. During completion of my research projects I designed and optimized several device architectures using numerical simulations and fundamental physical evaluation of sensing mechanism and performance. Fabricated devices were tested in custom built experimental setups in microfluidic testing chambers using automatic data measurement. Surface functionalization of device surface using self assembled monolayer techniques was employed for experiments that required specificity towards analyzed biological species.

Thesis Supervisor: Marc A. Baldo
Title: Associate Professor

Thesis Supervisor: Alexander van Oudenaarden
Title: Professor

Acknowledgments

I am thankful to my research advisor, Professor Marc Baldo for financial and academic support for a large portion of my doctorate. I would also like to thank my thesis co-advisor in the Physics Department, Professor Alexander van Oudenaarden in whose group I spend close to one year. The summer financial support and mentoring was greatly appreciated. To the rest of my thesis committee, Professor Sebastian Seung and Professor George Benedek, thank you for the time and comments related to my research.

I greatly enjoyed working with my colleagues. I thank Tim Heidel, with whom I worked on the organic semiconductor transistor sensors.

For the biosensor project, there are so many people I am indebted to: Kaveh Milaninia, for help building the experimental setup and all the clean room fabrication, Kemal Celebi, who developed the simulation software for both detector and light source, Jorge Zuniga, Colin Watson and Carlijn Mulder for their work on device fabrication, Liselotte Kaiser and Ky Lowenhaupt for help with surface plasmon resonance assays and instrumentation, Oktay Uzun for advice on self assembly and functionalization methods, Yong-Ak Song that shared expertise, materials and facilities for fabrication of microfluidic components.

I thank Priya Jadhav and Benjie Limketkai for insightful discussions on charge transport in organics, related to measurement of density of states, percolation theory and performance of the organic thin film transistor sensors.

I don't want to forget the rest of the group Jiye Lee, Mike Currie, Shlomi Goffri, Michel Segal and my colleagues next door with whom I collaborated on the carbon nanotube nano-fabrication project: Alfonso Reina, Hootan Farhat, Mario Hoffman, for advice related to nanotube growth and characterization, and Kaveh, for his help building the cold development experimental setup. I thank Luke Theogarajan for his availability to always take a critical look at my ideas and hypotheses.

My work could not have been completed without financial support from DuPont and the Institute for Soldier Nanotechnologies.

Finally, I thank my wife Emilia for her love, and the rest of my family for their support: Florin, Iulia, Iulian, Ilinca and my father, Patru. I dedicate this thesis to the memory of my mother, Maria.

Contents

List of Figures

List of Tables

Chapter 1

Motivation

Science and technology has progressed to measuring the environment in ways that extend well beyond the five basic senses in accuracy, physical properties, and limit of detection. Scientific discovery itself relies intrinsically on development of new sensing methods and tools. Of particular importance are sensors that measure chemical and biological species. Based on their operation mechanism, output, and application requirements, some sensors return a positive or negative value when a particular property exceeds a threshold value (the most common example being a carbon monoxide detector for chemical, or an off the shelf pregnancy test for biological species). Other uses require improved accuracy in measurement, as is the case of medical diagnostic tests, when analyte concentrations that fall outside an interval are indicative of a health hazard. In general, sensing is integrated in a feedback mechanism that alternates between measuring a state and altering it by external means. Pharmaceutical therapeutics cannot be administered without diagnosis and close monitoring of the effects. Sensor uses characterize not only presence but also complex interactions between species (e.g. binding kinetics) or even resolve some aspects molecular structure (e.g. antibody epitope mapping).

The research projects in this thesis cover chemical sensors based on thin film transistors, and biological sensors based on miniaturization of surface plasmon resonance sensors. For the transducing element both used organic semiconductors, chemical compounds of carbon that exhibit electrical conductivity that lies between that of metals and insulators. For the thin film transistor devices the conductivity of the organic layer is modulated by applying a gate voltage and the transistor characteristics show dependence on the molecular species present in the surrounding medium. The main advantage of the organic materials is that they are amenable to chemical modifications and one can envision design of materials that performed sensing tasks with improved selectivity and specificity. In addition, the large variety of organics provides a library compounds for device fabrication. The same principles are used in the most common chemical sensor found in the living world, the olfactory system. It exploits the large diversity of olfactory receptors, by far the largest family of receptors in the mammalian genome. It is estimated that as much as 2% of the mouse genome encodes olfactory proteins. The olfactory system concept was adapted to an electrical system consisting of an array of transistors, also known as electronic nose. The response of the array to an analyte provides fingerprint response the same way the biological system relays a complex sensation from the nasal organ.

Chemical sensors based on organic this film transistors are primarily driven by low cost applications that do not demand stringent sensing requirements as is the case of food industry monitoring in which quality control assurance is critical for public health. A typical example is spoilage of fruits or milk in which the detection system cannot exceed a small fraction of the total cost of the product.

Current biosensing methods were developed decades ago, independently of advances in the microelectronics field, and do not leverage on parallel fabrication, precision and reliability characteristic to semiconductor devices. The miniaturization of the surface plasmon resonance sensors described in this work aims at using functionalized solid state devices to detect biomolecular species in solution. The detection standards, ELISA (Enzyme Linked ImmunoSorbent Assay) and PCR (Polymerase Chain Reaction) rely on chemical amplification of either enzymatically processing a substrate into a measurable product or copying DNA strands. The consequence is that detectable levels take a significant time to accumulate (on the order of 3-4 hours), hence real time detection is not possible. Semiconductor devices do not need chemical amplification (although they can be used in conjunction with it) and real time detection can be achieved. Several device structures have been proposed for solid state devices for biological sensors: micro electro mechanical devices (MEMs), electrical devices (gated transistors, resistors), miniaturized fluorescence, and surface plasmon resonance assays[1]. While each method has its own drawbacks, the surface plasmon resonance seems to be the best candidate for successful replacement of current proteomic detection. MEMs used in aqueous environments (quartz crystal microbalance) suffer from significant dampening that decreases their sensitivity. A potential solution to this problem is a microfluidic channel embedded in a resonating cantilever. The sensitivity of microcantilevers increases with smaller device size, hence a need for more complex fabrication processes. Electrical devices have to resolve the fact that bio-molecular species have poor electrical properties and that typical biological buffers have high ionic strength that usually interact with the gating mechanisms. Optical detection (fluorescence and surface plasmon resonance) has the advantage of being most robust. Fluorescence detection requires labeling that increases the assay complexity and has the potential to disrupt the binding mechanism between molecular species. Sensitivity is usually not sufficient for routine laboratory tasks and is most often used in microscopy studies. For the electrical and optical devices considered the sensitivity is independent of the device length scale, under the assumption of uniform distribution of analyte, hence the device size can be chosen more conveniently.

Surface plasmon resonance sensors exploit the sensitivity of surface plasmons towards changes in the dielectric constant of media at a noble metal - dielectric interface. The reflectance of a gold film directly measures surface binding of proteins have a higher refractive index then the buffer in which they are dissolved. The main challenge for SPR is that changes in the refractive index are not always related to the binding assay. Of prime importance is precise control of temperature since the density (refractive index) of fluids depend linearly with temperature. The real time detection feature of SPR enables direct measurement of binding kinetics between the species immobilized on the surface and the one in solution. Surface plasmon resonance technology has its commercial uses in the research and development of the pharmaceutical industry for drug development applications. It is estimated that bringing a single new drug to market costs over $800 million and takes 10-15 years. Drug development starts with screening of huge compound libraries against bio-molecular targets responsible for diseases. The best candidates are selected based on the strength of interaction (binding) with the target that usually disrupts the disease progression pathway. The ability of SPR to measure directly the dissociation constant, the main indicative of binding strength, makes it the optimal technology for compound screening in drug development. In addition, the instrumentation can be easily automated for continuous operation.

The high price of SPR makes it suitable for applications in which high throughput is critical. Miniaturization of SPR aims at decreasing the cost of consumables and instrumentation so that the benefits of the technology can be introduced to users that do not support a high price point. Most obvious is the area of medical diagnostics that could benefit from a sensing method that is fast, economical, reliable and sensitive. The current diagnostics test, ELISA achieved a fairly low price point mainly due to processing in large batches at centralized locations, but suffers from slow detection speed. The present work on surface plasmons shows encouraging prospects towards making SPR a routinely used choice in a variety of research and industry settings.

Chapter 2

Review of surface plasmon resonance sensors and instrumentation

2.1 Introduction

Surface plasmons are electromagnetic waves that propagate along a metal dielectric interface. They are solutions to Maxwell's equations for transverse magnetic (TM) modes. On both sides of the metal and dielectric the electric field decays exponentially with distance. A surface charge density propagates along the boundary between the two media with a wavevector given by:

$$k_{pl} = \frac{\omega}{c}\sqrt{\frac{\epsilon_d \epsilon_m}{\epsilon_d + \epsilon_m}} \tag{2.1}$$

where ω is the angular frequency, c is the speed of light, ϵ_d and ϵ_m are the dielectric constants of the dielectric and metal. In order to have a positive wavevector k_{pl} the real part of the dielectric constant must be negative and its absolute value larger than the insulator dielectric constant. The condition is satisfied for most metals such as silver, gold, aluminum, copper, platinum. The existence of surface plasmons requires frequencies lower than a certain critical value, λ that depends on the plasma frequency.

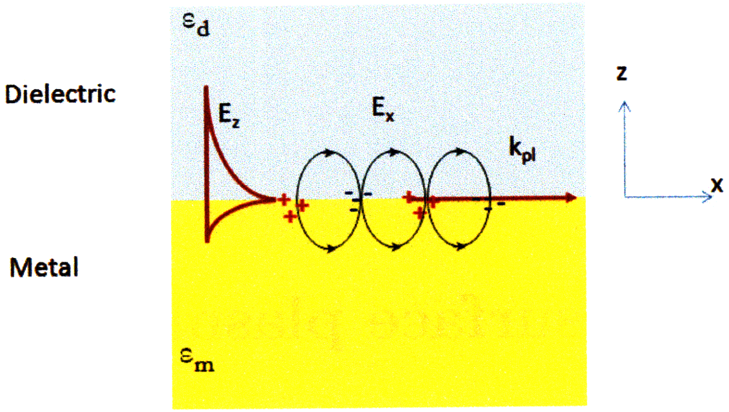

Figure 2-1: Plasmons are surface charge density waves propagating at a metal dielectric interface.

Plasma oscillation of surface electrons are coupled to electromagnetic radiation in several geometries. The Kretschmann configuration excites plasmons within a thin metal film placed between two insulators with different dielectric constants. The Otto configuration excites plasmons through the evanescent field of a total internally reflected beam. In this case a spacer layer between the coupling prism and metal film is present. Surface plasmons can also be excited on gratings when the horizontal momentum transferred by the diffracted light beam matches matches the momentum of plasmon waves. A particular case is plasmon coupling through surface roughness when the Fourier transform component of the wavevector matches periodicity conditions required by grating excitation. Metal nanoparticles also support surface plasmons excited by incident light, although it is important to notice that the plasmon dispersion relation is different from that of planar metal films.

The Kretschmann configuration for excitation of surface plasmons can be understood from the dispersion relations of both plasmons and light. Fig. 2-2 shows the $\omega(k)$ dependence for surface plasmons, and light in vacuum and an optical medium. The light propagating in vacuum and plasmon dispersion curves intersect only in origin, meaning that there is no physical solution for coupling between the two states. On the other hand the light line for denser medium has a smaller slope and inter-

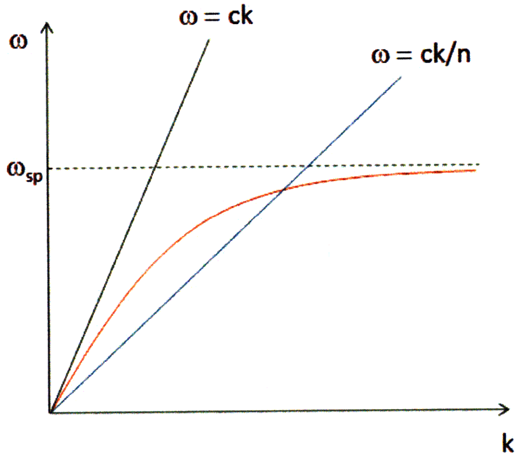

Figure 2-2: Dispersion relation for surface plasmons (red), light in vacuum (black) and light in an optical medium of refractive index n.

sects the plasmon curve in one additional point corresponding to surface plasmon resonance.

A typical experimental setup and results for plasmon excitation in the Kretschmann geometry is presented in Fig. 2-3. A laser beam falls on a gold film through an glass prism that has a refractive index higher than the immersion buffer. As the incidence angle is scanned, a resonant feature in the film reflectivity occurs when surface plasmons are excited beyond the total internal reflection angle between the glass and the buffer. The resonance location depends on the electromagnetic properties of the prism, metal layer and buffer.

When bio molecular species are absorbed on the metal surface the small changes in the dielectric constant change the resonance coordinate, hence measuring the reflectivity at the highest slope provides a means of monitoring real time binding kinetics. The sensitivity of the techniques is higher with narrow resonances, hence less lossy metals are preferable. While silver has the lowest plasmon full width half maximum (FWHM), in practice gold is preferred because it does not form a native oxide layer under common measurement conditions. It is important to notice that the shape of the resonance is asymmetrical with the right side having a significantly lower slope. The reflectivity (or amplitude) measurement is therefore performed on the left arm for a better signal to noise ratio.

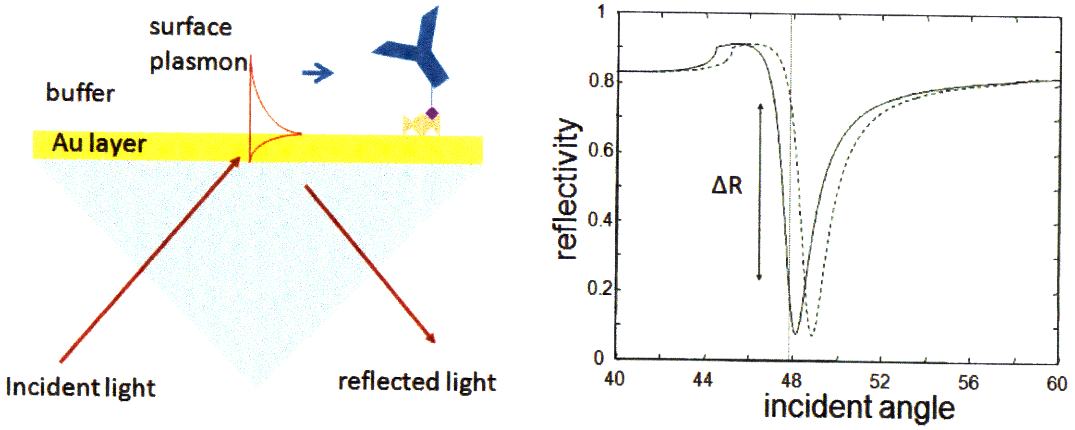

Figure 2-3: Surface plasmon excitation in the Kretschmann geometry. Surface plasmons are excited at the interface between the metal and low refractive index medium (left). A sharp dip in reflectivity is observed for angles of resonant energy transfer from incoming light into plasmon modes. The coordinate of the resonance depends strongly on the dielectric constant of the medium adjacent to the metal. Binding of biological species on the surface of the metal shifts the resonance towards higher angles and a change in reflectivity ΔR is measured to monitor analyte absorbance

The angular reflectivity spectra exhibit dips that correspond wiht the transfer of energy from the incident light wave into a surface plasmon and later dissipated in the metal film as heat. A SPR curve with minimal reflectivity as well as steep slope is observed for an optimal thickness of approximately 50 nm (Fig. 2-4). For gold films with a thickness larger than the optimal value, an SPR curve with a broader width, a higher minimum, a greater resonance angle,and a less steep slope is observed. For gold films with thicknesses greater than the optimal value, an SPR curve with a slightly smaller resonance angle, and greater reflectivity minimum is observed. The width and the asymmetry of the reflectivity dip increase with the decreasing metal thickness.

The surface plasmon resonance technique offers great sensitivity for molecules with relative high molecular weight, complemented by real time detection and no need for labeling that might interfere with the analyte biochemical functionality. Table 2.1 shows a comparison between SPR and other routinely used sensing methods[1]. In addition to excellent sensitivity, surface plasmon resonance offers real time detection,

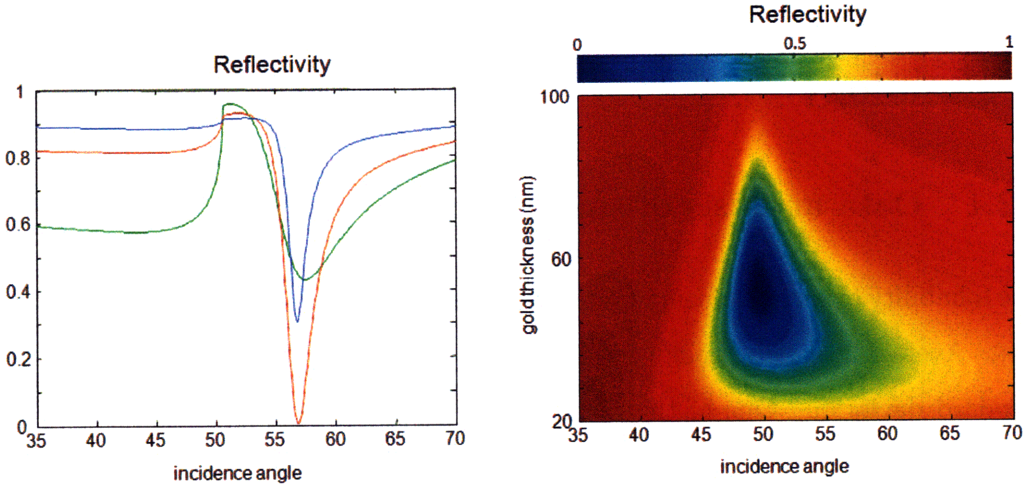

Figure 2-4: Reflectivity dependence of angle for a gold film of varying thickness. On the left, reflectivity curves of 30 nm (green) 50 nm (red), and 70 nm (blue) gold fim for a 670 nm incident light. On the right, a two dimensional plot for angular reflectivity for a gold film of variable thickness from 20 to 100 nm.

Table 2.1: Detection limits of protein and cellular sensing techniques.

Measurement technique	**Platform**	**Target**	**Sensitivity**
Surface Plasmon Resonance	Refractive index	Protein, Cell	10 pg/mm^2
Enzyme Linked ImmunoSorbent Assay	Absorbance	Protein	10 pM
Quartz Crystal Microbalance	Mass	Protein, Cell	1 ng/mm^2
Microcantilever	Mass	Protein, Cell	0.5 ng/mm^2
Polymerase Chain Reaction	RNA copies	mRNA	100 pg/ml
Immuno-Assay MultiPhoton Detection	Radioactivity	Protein	10 fg/ml

direct measurement of binding kinetics, integration with microfluidics for decreased sample size and increased throughput. The SPR assays do not use any labeling that might interfere with the biodetection mechanism.

In the past decade, surface plasmon resonance commercial instrumentation has been widely available from a variety of manufacturers (Biacore, GWC Technologies, Reichart Life Sciences, Bio-Rad Laboratores, ICx Nomadics), due to the fast adoption the technology.

2.2 Advances in surface plasmon resonance technology

2.2.1 Data analysis of surface plasmon resonance sensors

The reliability of surface plasmon resonance data depends on the accuracy of collecting data. Averaging n data points results in a decrease by a factor of $n^{1/2}$ in the noise standard deviation. One of the methods of finding the resonance minimum, called the centroid method, calculates the geometric center of the resonance minimum for data points above a certain threshold. Usually it does not coincide with the local minimum because the plasmon dip is asymmetrical. The final measurements are not affected since SPR experiments monitor relative shifts. When the light source intensity output fluctuates the spectrum is raised or lowered relative to the threshold value and the method leads to erroneous results due to resonance asymmetry. This shortcoming is solved by using an interpolating centroid tracking method. First, the data is interpolated so that the endpoints of the angular (wavelength) interval are assigned only a partial weight. Then the tracking interval is set to be roughly the full width at half minimum (FWHM). After the resonance shift the algorithm flollows the data curve and positions the tracking span such that the endpoints have equal value[52].

There are a variety of sources that change the output of an SPR sensor: analyte binding on the gold surface, temperature changes, mechanical instabilities, noise caused by the light source, detector or electronics. Usually, the largest contribution of noise comes from the photo-detector. It can be subdivided in several categories: shot noise (light intensity dependent) corresponding to fluctuations in the incoming light flux and carrier generation in the photo-detector, thermal noise, dark current noise, and readout noise of electronic interface. Typical charge coupled device (CCD) detectors achieve a resolution of $2*10^{-7}$ RIU (refractive index unit), and substitution with photo diode array (PDA) detectors achieve even higher detection limit of $2*10^{-8}$ RIU. The main challenges of low noise measurements are increasing the intensity of the light source and the throughput as typical SPR data points are collected every 1-5 s.

2.2.2 Signal referencing for improved SPR accuracy

A better signal to noise ratio and consequently improved stability and detection limit is achieved with parallel sensing channel architecture[31]. The incident light beam falls on a region divided in an active sensing layer and bulk background monitoring layer. The method allows for discrimination between bulk and surface effects and identify sample refractive index variations and non specific molecular binding.

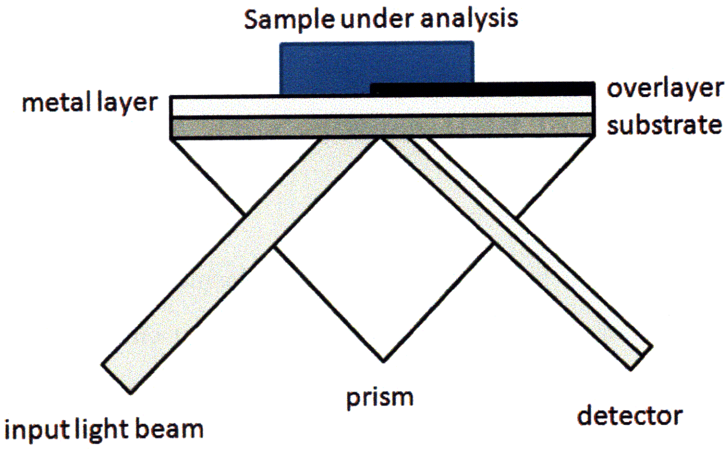

Figure 2-5: Dual SPR sensor with a tantalum oxide overlayer grown on top of the SPR active metal.

2.2.3 Surface plasmon resonance sensors based on phase detection

Most common SPR measurements are performed in the Kretschmann configuration at fixed angle of incidence and fixed wavelength and measure metal film reflectivity (amplitude). The Fresnel surface plasmon resonance model also predicts a rapid change in phase of the TM reflection that has a steep slope over a small range of refractive indices of the medium in the vicinity of the silver film[51, 60]. The sensitivity is comparable to that of amplitude SPR sensors in the range of $5 * 10^{-7}$ RIU. The theoretical model predicts that the phase change and sensor's dynamic range has a strong dependence on the thickness of the metal layer.

2.2.4 Surface plasmon resonsnce sensors for absorbing media

Surface plasmon excitation in the ATR (attenuated total reflection) configuration can be used to increase the absorbance of the sampled medium that can be explained due to an increased interaction length of plasmons along the metal plane[36]. As expected the optimal sensitivity silver thickness in the case of absorbing medium (48 nm) is lower than the one optimized for non-absorbing dielectrics (55.5 nm) for the 670 nm wavelength considered.

2.2.5 Integration of SPR sensors with Mach-Zehnder interferometer

Nikitin et. al. integrated a prism coupled surface plasmon resonance sensor into one arm of a Mach-Zehnder interferometer[55] Figure 1. An enhanced sensitivity is attributed to phase change shift and interferometric imaging provides spatial resolution on the micron scale that opens up possibilities for microarray imaging[73, 35]. A mixture of 0.001% of glycerol in water resolved a resolution of 10^{-7} RIU, attributed to the faster response of the phase to changes in the refractive index then that of the reflected intensity.

2.2.6 Long-range surface plasmons for high-resolution surface plasmon resonance sensors

Improvements in SPR sensitivity can be achieved by using long range surface plasmons (LSPR)[53]. The method uses thinner metallic films (20-40 nm) that are sandwiched between symmetric dielectric mediums. Since in the case of biological sensors one of the sides of the metal layer is exposed to aqueous solutions, a low refractive index buffer made of Teflon (n=1.31) or magnesium fluoride (n=1.38) is intercalated be-

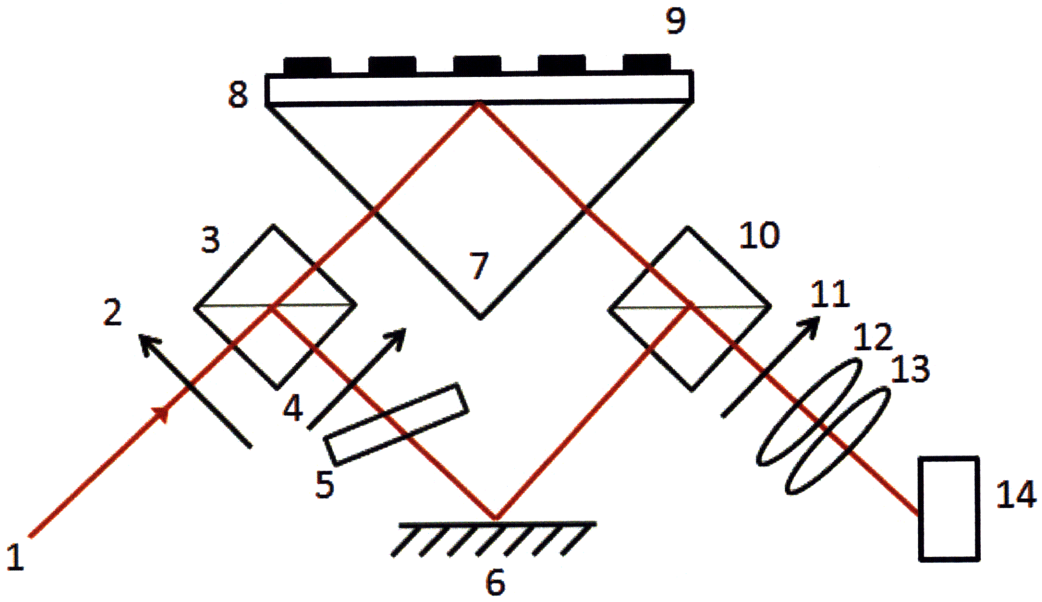

Figure 2-6: Experimental setup for integration of a Mach-Zehnder interferometer with a surface plasmon resonance sensor. Scheme of SPRI imaging: light beam (1), polarisers (2,4), beam-splitting cubes (3,10), phase-retarding glass plate (5), mirror (6), SPR prism (7), gold film (8), patterned coating (9), analyser (11), imaging lenses (12, 13), CCD camera (14).

tween the coupling prism and metal film. As the metal film decreases in thickness bellow 50 nm, surface plasmons will be excited on both surfaces of the film. Their interaction can be either symmetric (low losses, long propagation length) or anti-symmetric (high losses, short propagation length). The longer propagation length, or long range surface plasmons have a more narrow width and higher sensitivity then the conventional SPR.

Excitation of long range surface plasmons require dielectric media with similar refractive indices on both sides of a noble metal[71]. The dielectric buffer layer between the high index prism and metal film, Cytop (a fluoro polymer) can be spin coated to an 1180 nm thickness. A significant decrease in the resonance full width half maximum height is observed in the case of LSPR (FWHM=0.15 degrees) compared to conventional SPR (FWHM=1.2 degrees). Since the low thickness of dielectric buffer layer exceeds the light wavelength (814 nm), the plasmons are excited by the evanescent field of a total internal reflected light beam, the so called Otto configuration. The sharper profile of the long range plasmon resonance enables better sensitivity compared to the standard SPR approach. One of the drawbacks resides in the fact that long range plasmon penetration depth in the sampled medium (buffer) is larger than the conventional case of 200 nm. The LRSPR is used for imaging of DNA hybridization of microarrays chips and a detection limit of 5 nM is resolved for binding of a 16-mer single stranded DNA sample.

2.3 Optical fiber surface plasmon resonance sensors

2.3.1 Spectral fiber optic sensor based on surface plasmon resonance

A surface plasmon resonance miniaturized sensor is based on a fiber optic sensing element[62, 61, 30, 25]. The side of the fiber is polished to the core and a layer of gold of variable thickness (45-75 nm) is evaporated. The fiber transmission is measured over a spectral range of 750-950 nm and a minimum is observed for wavelengths that are coupled most efficiently into plasmon modes in the gold film. Upon changing the refractive index in which the sensor is immersed a shift in transmission minima of the optical fiber occurs. Further, it is shown that the shift depends linearly on the refractive index of the sampled fluid with a limit of detection of 5*10-7. A specific biochemical assay between human immunoglobulin (IgG) and monoclonal antibody against (IgG) measured shifts of up to 5nm.

2.3.2 Control of the dynamic range and sensitivity of a surface plasmon resonance based fiber optic sensor

In a variant of surface plasmon resonance sensors based on silica core optical fibers, gold is deposited at the tip around the stripped core[34]. A highly reflective silver

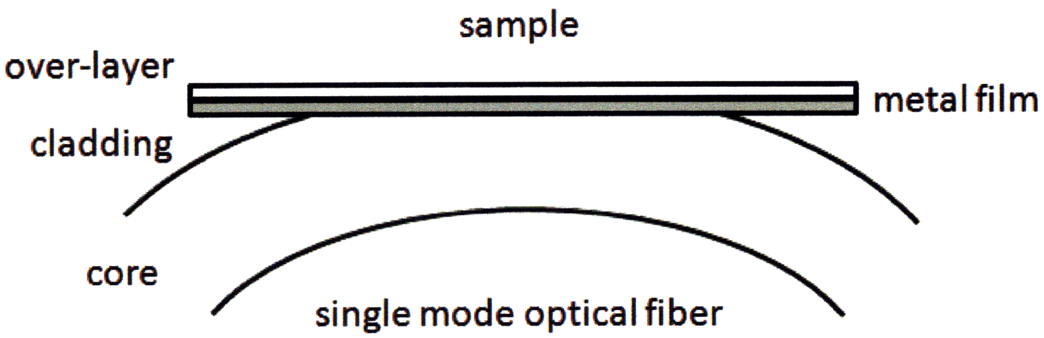

Figure 2-7: SPR sensor based on single mode polished fiber.

mirror is deposited on the flat polished end for signal enhancement. The wavelength response of fiber transmission provides medium limit of detection of $5 * 10^{-5}$ RIU with a dynamic range between 1.25 and 1.40. The dynamic range can be tuned to 1-1.33 with the addition of a high refractive index layer (zirconium oxide) deposited on the gold surface. A high refractive index core made of sapphire (n=1.77) shifted the dynamic range towards higher valued (1.45-1.72).

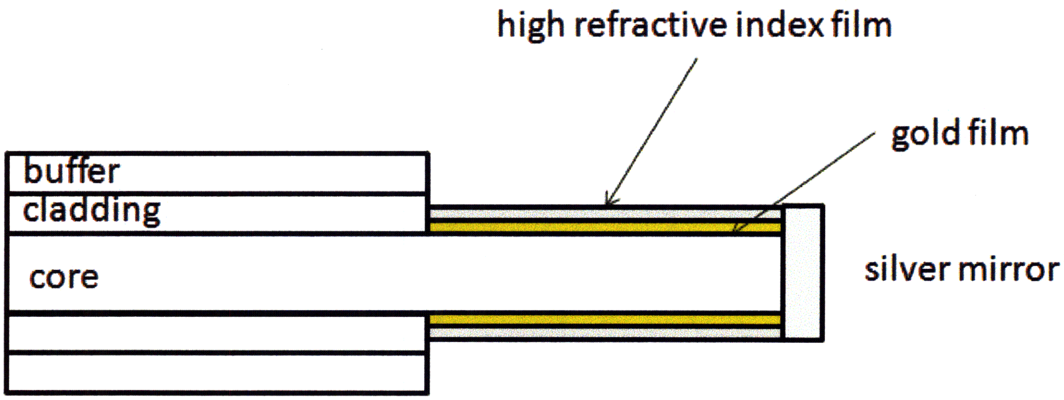

Figure 2-8: SPR fiber optic sensor with an optional high refractive index overlayer.

2.3.3 Optical fiber affinity biosensor based on localized surface plasmon resonance

Mitsui et al developed an optical fiber that uses gold nanoparticles immobilized on the flat polished tip of the fiber[48]. The instrument can measure the spectral response upon binding or monitor the back reflected light intensity in the fiber for a single wavelength excitation. In the amplitude measurement mode, the sensor shows great stability and a linear dependence between return light intensity and refractive index of the ambient medium. The device is tested to monitor binding kinetics of avidin on a biotin functionalized nanoparticle surface.

2.3.4 In-line fiber-optic sensors based on the excitation of surface plasma modes in metal-coated tapered fibers

A version of optical fiber surface plasmon resonance sensor uses a gold coated tapered fiber as an alternative to side or flat and polished fibers[24]. Symmetric or asymmetric metal coating devices can be used either wavelength or amplitude output sensors. The symmetric configuration excites plasmons with azimuthal order m=1, and are polarization insensitive, simplifying the sensor configuration and readout interpretation. The log of optical fiber transmission depends linearly on the refractive index of the immersion fluid.

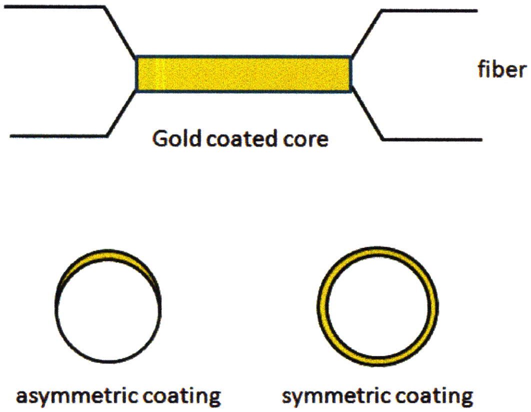

Figure 2-9: Schematic of gold tapered optical fiber sensor with asymmetric and symmetric metal layer.

2.3.5 Fiber optic sensor based on gold island plasmon resonance

A fiber optic based on gold island surface plasmon resonance is fabricated by stripping the cladding from a doped silica fiber, evaporating a thin layer of gold and annealing the device for 4 minutes at 800 degrees Celsius[46]. Annealing tends to shape the islands into spheres and shift the plasmon resonance towards lower wavelengths. The limit of detection is fairly low, 0.1 RIU, but the dynamic range is greatly improved.

2.4 Surface plasmon resonance sensors based on diffraction gratings

In addition to the attenuated total reflection geometry plasmons can be excited on diffraction gratings. After incidence on the grating the light is split into a reflected and diffracted beam of order m. A surface plasmon resonance phenomena occurs when the horizontal wavevector difference between incident and diffracted light matches the wavevector of the plasmon waves at the metal dielectric interface[26]. The light plasmon coupling efficiency increases with the amplitude of surface height modulation and decreases for higher diffraction orders. When the dielectric constant of the refractive index in the vicinity of the metal is changed, two symmetric plasmon dips are observed in the angular reflectivity of the film corresponding to diffraction orders m=1 and m=-1. Fabrication of diffraction gratings is based on photoresist exposure on a Mach-Zehnder interference pattern. After developer treatment the sinusoidal surface pattern is transferred onto a PDMS mold that was subsequently imprinted on a freshly spun UV curable polymer. After surface exposure to ultraviolet light the PDMS mold was peeled away a 50 nm layer of gold was evaporated. The sensor response measured as angle of resonance on a CCD detector array reach sensitivities of $5 * 10^{-6}$ RIU. Using multichannel multiplexed version of grating sensor device fabricated on inexpensive plastic substrates, an array capable of monitoring thousands of sensing spots was demonstrated[26].

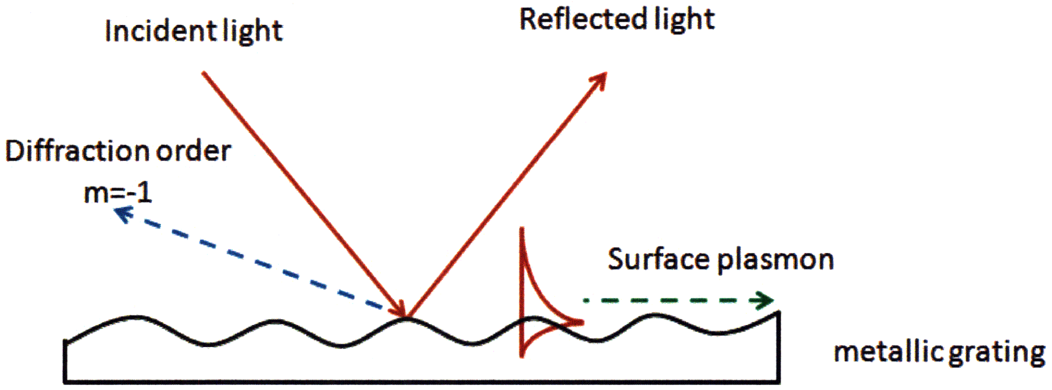

Figure 2-10: Excitation of surface plasmons on diffraction gratings. The momentum difference between the incident and diffracted wave is transferred to plasmon waves propagating at the metal dielectric interface. The reflected beam monitors the strength of the resonance.

2.5 Localized SPR: surface plasmons on metal nanoparticles

Siver nanoparticles were illuminated by a dark filed condenser and the light scattered by nanoparticles was collected by a microscope objective. The inverted microscope was equipped with an inverted spectrograph for recording the resonant Raleigh scattering spectrum of the nanoparticles[44]. The work demonstrates measurement of localized surface plasmon resonance (LSPR) on single silver nanoparticles that correlates into a zepto-molar range limit of detection. The system was used to measure the binding kinetics of 1-octanethiol self assembled monolayers and show a linear dependence between the Raleigh shift and the molecular weight of the species assembled on the surface.

In an article by Mock et. al.[50] silver nanoparticles were prepared by nucleating silver salts on 5 nm gold centers to an average diameter of 70 nm. The scattered light intensity profile is measured after immersion in oil with refractive indices from 1.44 to 1.56 and a linear dependence between LSPR shift and the index of the surrounding medium is observed. The sensitivity of the nanoparticles is dependent on their shape and plasmon resonance mode.

2.6 Integration of surface plasmon resonance instrumentation

A simple and compact realization of a SPR transducer was realized by using a laser diode that provides and angular spread and a linear photodetector array that captures reflectivity data for an interval of incident angles eliminating the need for mechanical rotational stages[43]. The sensor is used to detect concentrations of water in ethanol in the range of 0.3-10% and the temperature dependence of the signal from 20 to 25 oC was studied. Temperature compensated measurements with a reference channel provided analyte concentrations with increased accuracy over a range of working temperatures.

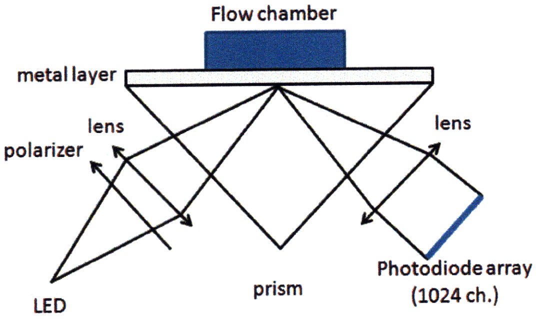

Figure 2-11: Schematic diagram of the integrated SPR sensor.

2.6.1 Spreeta

One of the most successful approaches to integration of surface plasmon resonance instrumentation was TI-SPR-1, co-developed between Texas Instruments and University of Washington[45]. The approach was to die mount and wirebond all electronic components: an AlGaAs narrow band LED and a diode array detector. After emission by the LED the light passes an aperture (to limit the angular spread that enters the system) and a polarizer (to limit introduction of TE modes that do not contribute to plasmon excitations). The light is incident on a surface plasmon layer (50 nm gold) and is reflected by a reflective mirror coating on a linear silicon photodiode array. An additional temperature sensor is included as refractive index of water changes approximately 10-4/1oC. The geometrical relationships between components is fixed providing mechanical robustness and no need for alignment and maintenance during use. The integration and miniaturization incorporates simplified optics for high volume manufacturability and low cost.

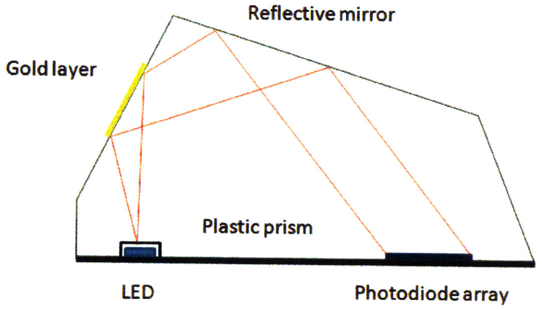

Figure 2-12: A schematic of the miniature surface plasmon resonance transducer TI-SPR-1.

The performance of Spreeta 2000 is discussed in terms of noise optimization techniques, accuracy and smoothness of the sensor[22]. For noise optimization the authors consider averaging and sum normalization and a detection limit of 1.8*10-7 is observed. The accuracy of the sensor is 0.2% over a change in RI of 0.04. The capabilities of the device are demonstrated by a binging assay for mouse IgG.

2.6.2 Waveguide surface plasmon resonance sensors

Harris and Wilkinson detail a theoretical evaluation of planar surface plasmon resonance waveguides[29]. The sensor measures optical transmittance through a rectangular optical waveguide whose evanescent field is coupled to surface plasmon modes on a planar metal film deposited across the waveguide. The transmission measured as the ratio between the outcoupled and incident power shows a sharp plasmon dip when plotted against the refractive index of the superstrate. The logarithm of transmission, $log(P_{out})$ was measured for a series of waveguides varying in plasmon waveguide length from 1.5 to 5.4 mm in steps of 0.1 mm and a linear dependence with the gold film length was observed. The sensor environment was changed from 1 (air) to 1.330

(water) to study the sensitivity of the sensor towards changes in refractive index of the superstrate. A more complex sensor design that uses a dielectric low refractive index buffer layer between the optical waveguide and the metal film offered greater sensitivity.

A sensor design optimized for use in an aqueous environment is presented by Harris et al[28]. An optical waveguide is coated with a thin metal film that supports surface plasmons interacting within the sensing region. The optical mode passed through a 3dB splitter. After propagating through either the sensing or the reference arm the modes exit through the signal or reference waveguide. The sensor is used to measure concentration of simazine over a 10-100 ng/ml range using an antibody assay. Limit of detection is measured as $1 * 10^{-4}$ RIU.

Chapter 3

Near field detector for integrated surface plasmon resonance biosensor applications

3.1 Abstract

Integrated surface plasmon resonance biosensors promise to enable compact and portable biosensing at high sensitivities. To replace the far field detector traditionally used to detect surface plasmons we integrate a near field detector below a functionalized gold film. The evanescent field of a surface plasmon at the aqueous-gold interface is converted into photocurrent by a thin film organic heterojunction diode. We demonstrate that use of the near field detector is equivalent to the traditional far field measurement of reflectivity. The sensor is stable and reversible in an aqueous environment for periods of 6 hrs. For specific binding of neutravidin, the sensitivity is three times lower than a comparable conventional SPR biosensor. The sensitivity of the near field detector can be further improved by reducing surface roughness of the gold layers and optimization of the device design.

3.2 Introduction

Despite widespread demand there remains an unmet need for cost effective biosensors. Applications in research laboratories, home and point of care diagnostics, process industries, environmental monitoring, security and bio-defense, require the measurement of bio-analytes with high specificity and minimal time lag between sample collection and measurement readout. Among commonly used sensing methods, surface plasmon resonance (SPR) achieves relatively high sensitivity (0.5 ng/cm^2) [1], and provides the benefits of label free detection and real time measurement of binding kinetics, while integration with microfluidics reduces the sample size and enables high throughput [2]. SPR biosensors are highly versatile tools, being routinely used to examine protein - protein, antibody - antigen, and receptor - ligand interactions [3]. However, they are also large, difficult to transport and relatively costly, due to their dependence on precise calibration and alignment of the internal optics.

The disadvantages of SPR biosensors could be overcome by integrating the devices in solid state. As in other optical applications such as lasers, solid state integration can significantly reduce the footprint of the device, and improve the environmental stability in the presence of vibrations and temperature changes. The resulting device contains three components: an optical pump, a near field detector for surface plasmons, and an aqueous interface with the bio-analytes.

In this work, we demonstrate integration of a near field surface plasmon detector [4] and the biorecognition interface of a traditional SPR sensor. The near field detector is used to replace the conventional far field optical detector. It is integrated directly with an Au/water interface that supports surface plasmons and acts as the binding site for bio-analytes. The integration of the optical detector is arguably the key challenge confronting the integration of a SPR biosensor. The remaining optical element, the optical pump, can be replaced by a microcavity light emitting diode (LED) [5, 6], or vertical cavity surface emitting laser (VCSEL) [7], placed under the near field detector and tuned for the wavevector of the plasmon resonance. Integration with an LED or VCSEL is not performed here, instead the integrated detector is characterized using an external laser.

3.3 Results and Discussion

Conventional SPR sensors consist of a gold film deposited on glass and immersed in water [2]. The system is optically excited through the glass by a pump laser. When the angle of the laser beam incident on the Au/water interface hits the resonance, surface plasmons are generated at the Au/water interface and the reflected light drops markedly. The resonant angle is a sensitive function of the refractive index of all media within the range of the surface plasmon - typically $\sim$50 nm in Au and $\sim$200 nm in water. Thus, analyte binding events at the Au/water interface modify the coupling of light into the surface plasmon and are detected from variations in the optical reflectivity.

We seek to replace the far field measurement of reflected light with a direct near field measurement of the surface plasmons themselves [4]. The sensitivity of conventional SPR sensors is maximized for an approximately 50-nm-thick layer of Au deposited on glass [8]. But the electromagnetic field is negligible at the bottom of the 50-nm-thick Au layer, preventing near field detection of the surface plasmons below the Au. Thus, to efficiently detect surface plasmons at the aqueous interface with minimal change in sensitivity, we split the gold layer and insert a semiconductor; see Fig. 3-1.

To determine the ideal properties of the semiconductor, we calculate the sensitivity of a model near field SPR detector. The top and bottom gold layers are 20-nm-thick. The top surface of the device is immersed in buffer with a refractive index $n=1.38$. The substrate is glass with a refractive index $n=1.72$. The Poynting vector within the model device is calculated using a transfer matrix method assuming plane wave incident light [5]. To detect the surface plasmon in the near field the semiconductor must exhibit strong optical absorption. We assume that the semiconductor is 50-nm-thick with an extinction coefficient $k=0.2$. The sensitivity of the detector is calculated from the relative change in absorption within the semiconductor given the

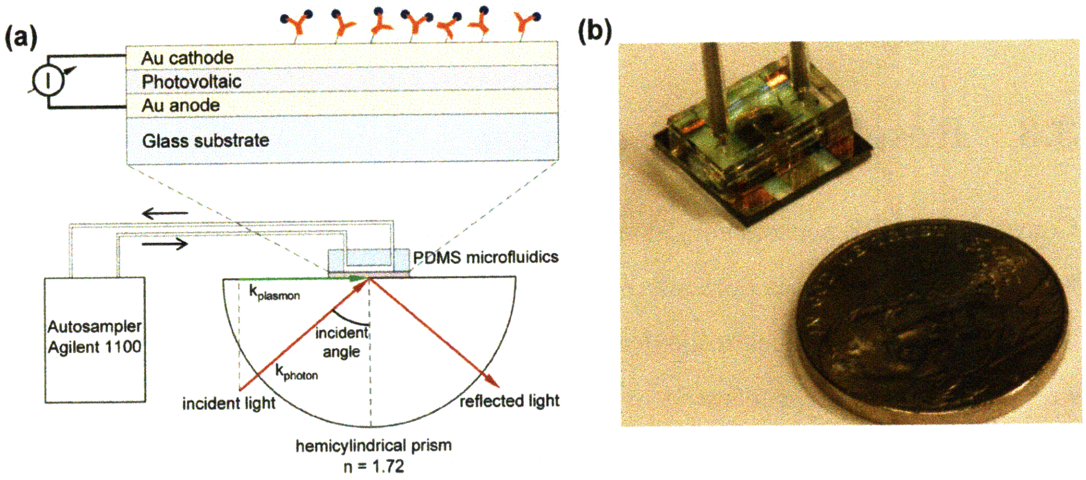

Figure 3-1: (a) Device structure and experimental setup. The near-field surface plasmon detector consists of a thin layer of a semiconductor sandwiched between two thin gold electrodes. The top gold electrode is circular with a radius of 1 mm. The top gold electrode defines the area of the detector and acts as the analyte binding surface. Biological materials are supplied by an autosampler through a microfluidic circuit. A p-polarized beam from a 1 mW laser at λ=670 nm is aligned with the detector. The incident angle of the beam is adjusted by rotating the hemi-cylindrical lens with the detector attached. The reflected light and device photocurrent are monitored as a function of the incident angle and binding events on the top gold surface. (b) Photograph of a device integrated with a PDMS microfluidic chamber and connecting tubing. A US quarter is also shown to illustrate the scale of the detector.

introduction of an interfacial 5-nm-thick protein layer with refractive index n=1.40.

As shown in Fig. 3-2, we find that the sensitivity of the model device is maximized for semiconductor refractive indices between n=1.3 and n=1.8. The relative change in absorption within the semiconductor is 30% for the optimal choice of refractive index. When combined with the requirement for strong optical absorption, this calculation supports the choice of organic semiconductors for this application. For example, the archetype organic photovoltaic material copper phthalocyanine (CuPC) exhibits n=1.7 and k=0.2 at λ=650 nm.

To compare the sensitivity of the near field detector to that of a conventional SPR, we also calculated the relative change in reflection from a 50-nm-thick Au layer. The same 5-nm-thick protein later with refractive index n=1.40 causes a 60% change in reflection, suggesting that the near field detector should exhibit roughly

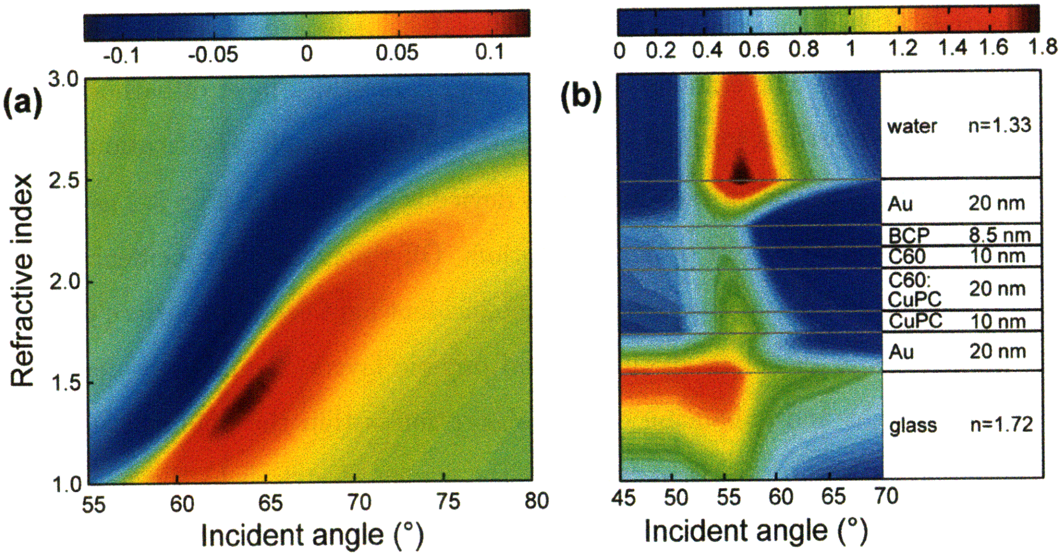

Figure 3-2: Simulation of the sensitivity of a near field surface plasmon detector as a function of the refractive index of the semiconductor material. The sensitivity is estimated from the change in photocurrent following the simulated binding of a thin protein layer on top of the device. It is plotted as a function of incidence angle of the optical source for a 50-nm-thick semiconductor with extinction coeffcient k=0.2 sandwiched between two 20-nm-thick gold layers. Higher sensitivity is achieved for lower refractive index materials, making organics a suitable candidate for plasmon detector applications. The maximum absorption in the photovoltaic is 0.4, hence the relative change in absorbance is 30% (b) Structure of the near field surface plasmon detector and simulated amplitude of the electric field for the transverse magnetic mode within the device. Surface plasmon excitations have the highest amplitude on the top surface of the cathode layer but they also extend into the organic layers of the photovoltaic. Energy from the plasmonic mode is channeled into formation of excitonic states that dissociate at the hole and electron transport layer interface.

half the sensitivity of a conventional device. The calculated sensitivity of the near field detector should not be considered as a limit, however, since its structure contains opportunities for design optimization. For example, the bottom Au contact can be replaced by a lower loss Ag electrode.

Consistent with the refractive index guidelines of Fig. 3-2, we design a practical organic semiconductor-based photovoltaic detector. The anode is a 20-nm-thick gold layer. The donor material within the organic photovoltaic is a 10-nm-thick film of CuPC. The acceptor material is a 10-nm-thick film of buckminsterfullerene (C_{60}). To increase optical absorption, a 20-nm-thick bulk heterostructure consisting of a

1:1 mixture of the donor and acceptor materials is deposited between the donor and acceptor layers. The cathode consists of an 8.5-nm-thick layer of bathocuproine (BCP) and a 20-nm-thick top gold layer. See Methods for complete fabrication details.

The electric field within the CuPC/C_{60} device is simulated in Fig. 3-2 as a function of the incident angle of optical excitation. Off resonance, the incident light is primarily reflected. But at the resonance, the incident light excites a surface plasmon that propagates in the plane of the Au and organic layers, significantly decreasing the reflected light and enhancing optical absorption within the photovoltaic. This enhancement in absorption is apparent in the strong electric field throughout the organic layers at the resonance condition.

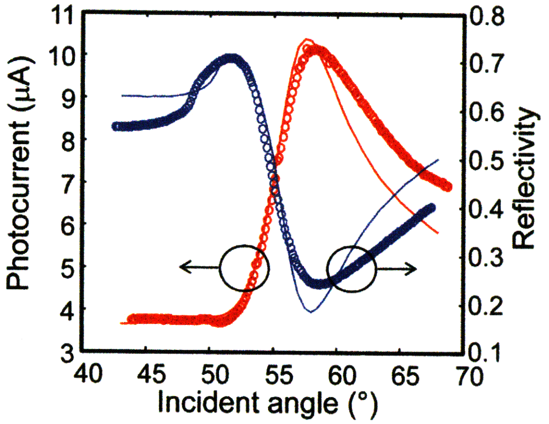

Figure 3-3: The angular dependence of the photocurrent from the device (red circles) and reflectivity (blue circles). The solid lines represent transfer matrix numerical simulation for photocurrent (red) and reflectivity (blue) using n and k data measured for the materials used in device fabrication. The discrepancy between simulation and the data is most likely due to surface roughness in the gold electrodes.

The dependence of the photocurrent and reflectivity on the angle of incidence of the incoming light is measured and compared with the simulation in Fig. 3-3. Devices were immersed in a saline buffer (HEPES, GE Healthcare, Piscataway, NJ) typical of biosensing applications and exposed to a 1 mW laser at $\lambda = 670$ nm; see Methods. Both data and simulations show an increase in photocurrent and a decrease in reflected light at the resonance condition (approximately 58°). The photocurrent at the surface plasmon resonance is approximately two times higher than the off resonance baseline due to enhanced absorption. We conclude that the reflectivity and photocurrent are equivalent measures of surface plasmon generation. However, the resonance width for the experimental plots exceeds the theoretical prediction, slightly lowering the sensitivity. The discrepancy is likely due to the 10 nm surface roughness of the Au layers within the device. Surface roughness lowers sensitivity by enhancing scattering of the surface plasmons, which decreases their lifetime and hence increases the angular width of the resonance [9]. The scattering losses could be alleviated by careful preparation of the Au surfaces.

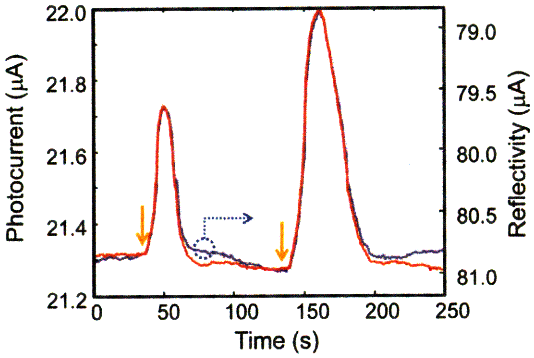

Figure 3-4: Sensor exposure to two water pulses in HEPES buffer flow. Both reflectivity and photocurrent are modulated when the bulk dielectric constant of the medium above the device is decreased. The sensor shows excellent reversibility and stability.

Next, the sensor response is examined within a microfluidic system; see Methods. To test the stability, sensitivity and reversibility of the sensor, water pulses of 30 and 60 s in length are injected into a constant flow of HEPES buffer. As shown in Fig. 3-4, the slight change of refractive index during the water pulses is detected by the sensor. We observe a simultaneous change in reflectivity and current with proportional amplitude of the two quantities. The sensor shows reversibility at the end of the water pulse and good stability with negligible drift of the baseline. The water pulse response was tested for several incidence angles for the incoming light to find the maximal sensitivity angular coordinate for later binding assays. Next, we performed a specific binding assay for biotin-neutravidin, an archetypal evaluation of sensing platforms. The surface of the sensor was first immersed in water for 2-3 hours with a 5:1 molar mixture of PEG (polyethylene glycol) acid disulfide and biotin PEG disulfide (Polypure, Oslo, Norway). The purpose of the functionalization is to space out the biotin moieties to avoid steric hindrance and spatial overlap between neutravidin binding sites [10]. The PEG backbone prevents protein absorption on Au, minimizing non specific interaction with the surface [11]. Normally, this functionalization is performed in ethanol because functionalization in water decreases the surface coverage due to the hydration volume around the ethylene glycol moieties. The removal of water from the polyethylene glycol chains is thermodynamically unfavorable, and it prevents close packing of the polymer as well as surface access to protein species present in solution [12]. But the water-based assembly is necessary here because the organic photovoltaic materials are weakly soluble in ethanol. Higher sensitivity could be obtained for surface functionalization with carboxyl methyl dextran hydrogel, which contains more binding sites for neutravidin within the range of the surface plasmon [13].

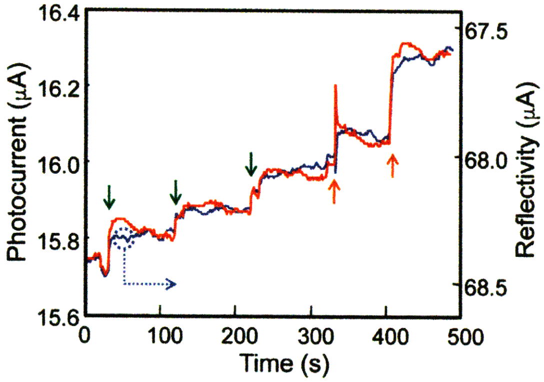

Figure 3-5: Sensor response to casein and neutravidin. Green arrow: exposure to casein to block non-specific binding sites, orange arrow: specific detection of neutravidin. Both species bind irreversibly to the surface. The data demonstrates that the photocurrent response of the near field surface plasmon detector is equivalent to the conventional measurement of reflectivity.

For selective detection of neutravidin, any remaining non specific binding sites on the Au surface were passivated with a 1 mg/ml solution of casein [14]. Then, in a constant flow of 250 μl/min HEPES buffer, the sensor was exposed to sequential pulses of 250 μg/ml neutravidin (Pierce Biotechnology, Rockport, IL) of 125 μl injection volume each. Figure 3-4 shows a simultaneous response in the reflectivity and short circuit current when casein and neutravidin bind irreversibly to the functionalized surface of the sensor. The sensitivity of the near field device is 4 μg/cm^2. We performed the same binding experiment using a conventional reflectivity-based detection of surface plasmons on a 50-nm-thick gold layer, except that the surface functionalization was performed in ethanol. We obtained a sensitivity from the conventional approach that is approximately three times better than the near field detector. From the theoretical analysis accompanying Fig. 3-2 we expected a factor of two difference in sensitivity. The additional loss in the near field detector is likely due to inferior surface functionalization because of the restriction to water rather than ethanol.

Nevertheless, the relative similarity in sensitivities suggests that near field detection can be employed in the majority of applications for surface plasmon resonance detectors. Finally, we consider the stability of near field surface plasmon detectors. Illumination is typically applied to contemporary biosensor chips for no longer than a few hours [8]. Thus, we expect that the stability of organic photovoltaic cells is sufficient for application in solid-state SPR detectors. The shelf life must be much longer than the operation life, but encapsulated organic photovoltaic cells have exhibited shelf lives exceeding 6000 hours [15]. Our devices were not encapsulated and were tested within 24 hours of surface functionalization. We observed stable photocurrent throughout the 6 hour duration of our experiments with the top gold layer immersed in a saline buffer. Submerging the sensor in saline buffer solutions does not affect the electrical performance. In all cases the gold contact where the binding takes place was grounded. Diode characteristics in either air or buffer remained unchanged for anode bias in the -1V to +1V region, indicating that there are no leakage currents in solution. Although we did not observe stability problems in our experiments, C_{60} is known to exhibit photo-induced degradation in the presence of oxygen [16]. Consequently, we also experimented with another acceptor, 3,4,9,10-perylene tetracarboxylic bisbenzimidazole (PTCBI). The combination of PTCBI and CuPC forms extremely stable photovoltaic devices. We observed similar device performance from PTCBI/CuPC, however, we found the use of PTCBI significantly increased the density of short circuit defects in these relatively thin devices.

To conclude, conventional SPR detectors measure the optical reflection in the far field. In this work, we replace the far field detector with a near-field detector positioned below the Au binding surface. The correlation between far field reflectivity and photocurrent from the near field detector observed in Figs. 3-3, 3-4, 3-5 demonstrates that the near field detectors can replace the traditional far field approach. We observe a factor of three decrease in the sensitivity of our near field detector compared to a conventional SPR detector. In theory, the near and far field approaches should yield comparable sensitivity upon binding of biological species on the surface. But in practice our near field detector is affected by incomplete surface functionalization and surface plasmon propagation losses that compete with absorption in the organic semiconductors. Possibilities for improving the sensitivity include using longer wavelength light, the selective replacement of Au by Ag, and reductions in surface roughness of the metal layers. When combined with a microcavity LED or VCSEL, the near field detector should allow the integration of SPR biosensors into thin film devices, improving portability and environmental stability, potentially lowering costs, and introducing a new approach to the unsolved problems of biosensing.

3.4 Sensor fabrication and experimental setup

Devices were fabricated using thermal evaporation under vacuum ($\sim 10^{-6}$ Torr). First, a 20-nm-thick gold anode with a 3-nm-thick chrome adhesion layer was deposited through a shadow mask onto a flint glass substrate (SF10 glass, Schott AG) with a refractive index n=1.72. The organic photovoltaic materials CuPC, BCP, C_{60} (Sigma-Aldrich, St. Louis, MO), and PTCBI (Sensient Imaging Tech Gmbh, Wolfen, Germany) were used after thermal gradient purification [17]. The 20-nm-thick top gold contact was patterned using a shadow mask. The active area of the device is approximately 0.79 mm^2. After fabrication, the photovoltaic cells were optically coupled using an index matching fluid (Cargille Laboratories) to a hemi-cylindrical prism made from the same material as the substrate (SF10 glass, Schott AG). The prism was mounted on a translation stage (Thorlabs, Newton, NJ) above a motorized rotation stage (AF Optical, Fremont, CA) aligned so that the motional rotation axis coincides with the symmetry axis of the cylindrical prism. The active region of the sample was placed on the prism axis and a λ=670 nm laser beam was collimated, p-polarized and focused on the same active region. The incident angle of the incoming laser beam was varied by rotating the prism. The angular dependence of the photocurrent and the reflectivity as monitored by a silicon photo-detector, were measured with a Keithley 2602 dual source-meter. For simulation purposes, the refractive indices and extinction coefficients of the gold used in the calculation were measured using an Aquila nkd-8000 (Aquila Instruments Ltd., Blackburn, UK).

3.5 Microfluidics

Microfluidic masters were made of 2150 SU-8 negative photoresist (MicroChem Corp., Newton, MA), spun at 2000 rpm on a piranha cleaned silicon wafer for an expected thickness of approximately 0.28 mm. The wafer was soft baked in a convection oven for 7 minutes at 65 °C for thermal stress reduction followed by a 90 minute bake at 95 °C. The photoresist was patterned through a chrome mask by ultraviolet light exposure with a 370 mJ/cm^2 dose, baked for 5 minutes at 65 °C and 30 minutes at 95 °C. Development was performed on a spinner with SU-8 developer until all unexposed material was removed. PDMS molds (Sylgard kit, Dow Corning, Midland, MI) were made with a mixture of 10:1 elastomer to primer ratio that was baked overnight at 65 °C. The rest of the microfluidic components, tubing, manual valve, adapters and connectors were purchased from Upchurch Scientific (Oak Harbor, WA). The final volume of the flow chamber was 1.2 μl, while tubing and connectors accounted for 3 μl.

All the sensing and binding measurements solutions were delivered to the surface of the sample using an Agilent 1100 HPLC autosampler. Exposure to water and biomolecular species was performed in step functions of various temporal lengths by adjusting the flow rate (250 μl/min) and the injection volume (125 μl). Before and after each injection of water, casein and neutravidin, the device was rinsed thoroughly in a buffer identical with the one used to dilute the biological samples. Although square water pulses are sent from the injection coil of the autosampler, the device response indicates that the pulse is modified by diffusion and parabolic flow patterns inside the connecting microfluidic tubing and chamber. Reflectivity and photocurrent were sampled with a period of 1 second.

3.6 Binding kinetics of analytes

A first order kinetic model is employed for binding of biological species on the surface of the sensor. For simplicity, it is assumed that there is no distinction between specific and non-specific binding sites or that the latter ones are fully passivated by a preliminary surface treatment. The time evolution of the concentration of analyte interacting with the surface is described by:

$$\frac{df}{dt} = k_a c(f_{max} - f) - k_d f, \tag{3.1}$$

where f is the number of occupied binding sites, c is the concentration of the injected analyte near the surface, f_{max} the total number of available sites and k_a and k_d the association and dissociation sites with units of ($M^{-1}s^{-1}$, and s^{-1}). The rate equation between neutravidin and biotin modified surface can be simplified since the dissociation rate is negligible:

$$\frac{df}{dt} = k_a c(f_{max} - f), \tag{3.2}$$

Under ideal exposure of the sensor to step function concentrations of neutravidin the current and reflectivity response should follow an exponential curve.

Chapter 4

Integrated surface plasmon resonance biosensor based on organic semiconductor devices

4.1 Introduction

In this chapter we propose a new biosensor design that integrates a plasmon pump and detector. An organic light emitting device (OLED) excites plasmons in a near field detector, all integrated in a vertical structure. The plasmon detector is a photovoltaic heterojunction that converts plasmonic waves into excitons that dissociate at the interface between hole and electron transport layer, therefore the short circuit current measured across the detector is proportional to the amplitude of plasmon excitations. The sensitivity of the plasmons towards changes in the dielectric constant of the medium adjacent to the surface of the detector upon biological binding is the basis of detection. Further, surface functionalization with self assembled monolayers and covalent binding of antibodies leads to specific detection. While typical surface plasmon resonance detection schemes rely on an external light source coupled with an angular prism, our design uses a resonant cavity angular emission OLED to excite plasmons in the detector. Fig. 4-1 shows the structure of such a device.

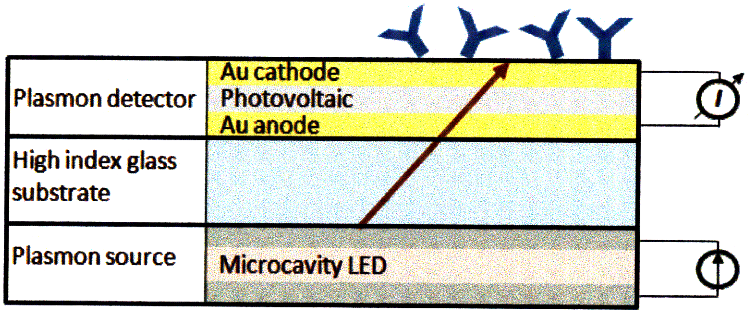

Figure 4-1: Integrated surface plasmon resonance biosensor consists of a microcavity OLED with off normal angular emission intensity profile, a high index substrate and a plasmon detector sensitive to binding events on the surface of the sensor.

4.2 Results

The OLED and photovoltaic detector were fabricated by thermal evaporation under vacuum (at 10^{-6} Torr). Layer composition and thicknesses for each device is indicated in Fig. 4-2 and Fig. 4-3. The contacts were patterned with shadow masks and organics were blanket evaporated. Both OLED and detector have an active area of 0.79 mm^2.

The OLED's anode is a semitransparent layer of silver and the cathode is a highly reflective Al/LiF layer. The electron transport layer is 2,9-dimethyl-4,7-diphenyl-1,10-phenanthroline (bathocuproine or BCP), 42 nm thick. The hole transport material is N,N'-diphenyl-N,N'-bis(3-methylphenyl)-[1,1'-biphenyl]-4,4'-diamine (TPD). To facilitate hole injection from the silver anode and to decrease the overall resistivity of the OLED the first 162 nm were doped with 2% by mass of tetrafluorotetracyanoquinodimethane (F4TCNQ). The emissive layer consists of 6% red emitting dye 2,3,7,8,12,13,17,18-octaethyl-21H,23Hporphine platinum(II), (PtOEP) doped in a 46 nm 4,4'-N,N'-dicarbazole-biphenyl (CBP) host layer. The angular emission profile is adjusted by changing the thickness of the doped TPD layer. When the emission wavelength of the dye, λ_{dye} matches the optical length of the cavity or cavity optical length, $n_{cav}d_{cav}$, light will be emitted through the top mirror perpendicular to the surface of the OLED. In the situations in which the OLED is positively detuned (i.e. $n_{cav}d_{cav}$ is greater than λ_{dye}), due to the periodicity condition for normal component of the light wave vector, light is emitted at an angle given by the optical parameters

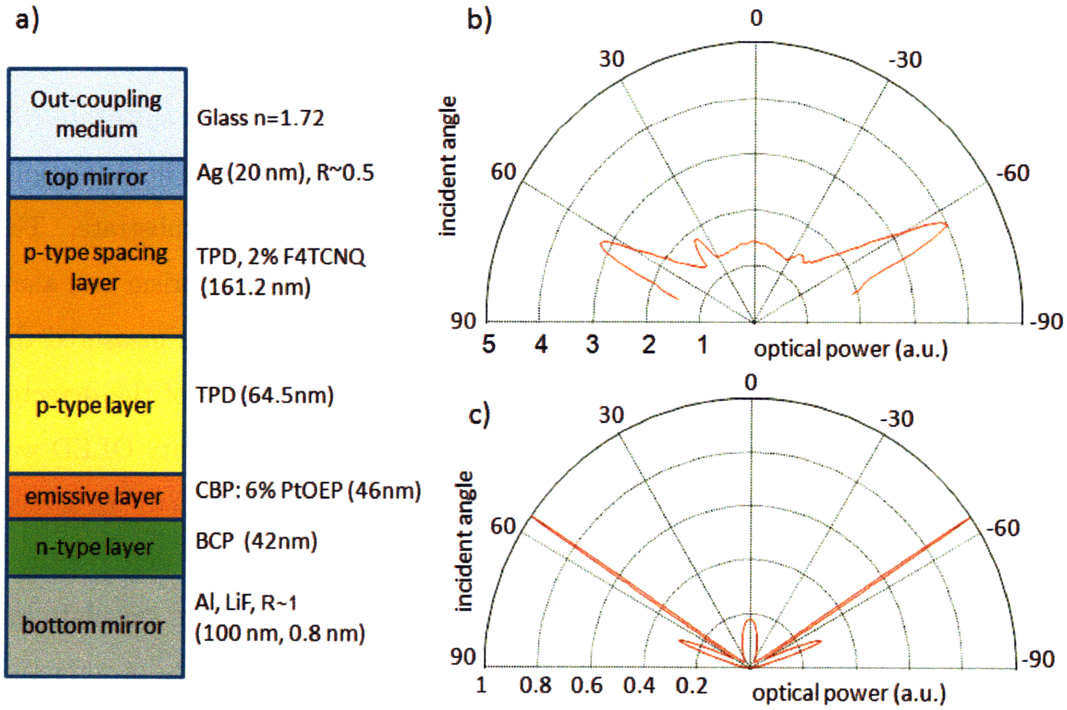

Figure 4-2: a)Device structure of the resonant cavity angular emission OLED. The top contacts form two mirrors with reflectivity coefficients R=1 for the bottom and R=0.5 for the top. The length of the cavity is adjusted by varying the p-type spacing layer of TPD doped with 2% F4TCNQ. b) Experimental measurement of the angular intensity profile of the light emission from a resonant cavity OLED. The length of the cavity is adjusted such that the intensity of emitted light is maximum off normal. c) Numerical simulation of the OLED output light intensity calculated using directly measured n and k values for the organic materials in Fig. 4-2(a). The discrepancy between the angular coordinate of the maxima is attributed to measurement error of material properties (n, k).

of the structure:

$$\theta = sin^{-1}\left(\frac{n_{out}}{n_{cav}}\sqrt{1-\left(\frac{\lambda_{dye}}{\lambda_{dye}n_{cav}}\right)^2}\right) \tag{4.1}$$

where θ is the angle the light emission, n_{out} and n_{cav} is the refractive index of the out-coupling and cavity media. The OLED layer thicknesses were tailored to outcouple emission in glass at around 60 degrees for optimal excitation of plasmons in the near field detector. In Fig. 4-2(a) we show the structure (materials and thicknesses) of an angular emissive OLED. In order to adjust the angle of light the p-type spacing layer (TPD doped with F4TCNQ) was varied while keeping all other layers unchanged. Fig. 4-2(b) shows a measurement of light intensity profile for a 650 nm PtOEP OLED. The OLED was deposited on a high index glass substrate (SF 10, Schott AG) that was later optically coupled with index matching fluid (Cargille Labs) to a cylindrical prism made from the same material as the substrate. The active region of the OLED was placed on the symmetry axis of the prism and a silicon photodetector (Newport) placed on a motorized rotational stage measured the intensity of the emitted light. We estimate that the spatial length of the detector increases FHWM of the angular profile by 3-5 degrees. The microcavity OLED was designed using an analytical model that determines the Poynting vector in a multilayer organic device. The optical constants n and k of each layer were obtained using a spectrophotometer Aquila Instruments nkd8000. Further, we calculate the angular dependence of emitted power in a semi-infinite glass substrate of refractive index n=1.72. Fig. 4-2(c) shows the predicted emission of the OLED structure in Fig. 4-2(a), averaged over all spatial orientations of the emissive dipoles.

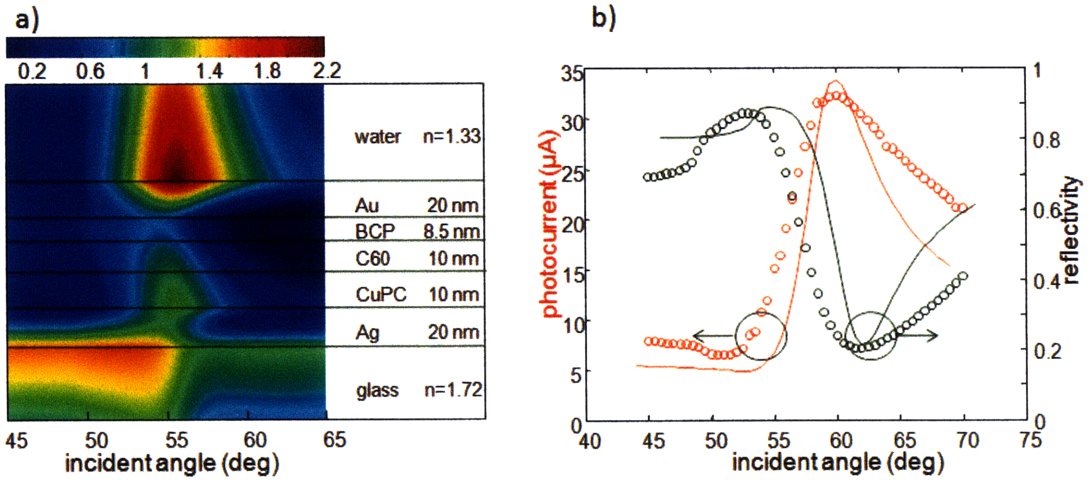

Figure 4-3: a)Electric field profile throughout the plasmon detector structure. b) Reflectivity and photocurrent for the considered device.

Detector devices consisted of a bulk heterojunction diode with 20 nm C60 as electron transport layer and 20 nm CuPc as hole transport layer (Fig. 4-3). An exciton blocking layer BCP was evaporated to increase the photovoltaic efficiency.

The thicknesses of contacts were 20 nm gold for anode and 20 nm silver for cathode. While a device both contacts made of silver provides a better sensitivity for the same amount of analyte bound to the surface of the sensor we opted for a gold contact at the interface with the aqueous sample because of higher quality of self assembled monolayer functionalization.

Simulation of the electric field amplitude, photocurrent and reflectivity plots were calculated using a transfer matrix method to determine the electric field and Poynting vector at every point within the multilayer structure assuming plane wave incident light. The refractive indices and extinction coefficients for the films used in the modeling were directly measured using an Aquila nkd-8000 thin film measurement instrument. Fig. 4-3(a) illustrates the presence of plasmonic states for the transverse magnetic mode. While for single gold layers with thicknesses above 50 nm these states are confined to the interface between gold and water (data not shown), in the case of metal contacts photovoltaic hetero-structure the plasmonic states span the entire device. At incidence angles that excite plasmon modes on the device, higher electric field amplitudes inside the organic semiconductors layers are observed as compared to off resonance angles.

Fig. 4-3(b) shows reflectivity and photocurrent plot for a near field detector deposited on a high index glass substrate composed of 20nm Ag, 20 nm CuPc, 20 nm C60, 8.5 nm BCP, and 20 nm Au. Photocurrent and reflectivity dependence on the angle of incidence of the incoming light were monitored to test the organic diode as a plasmon detector. The reflectivity is measured to probe surface plasmon waves in the device as a sharp dip in reflectivity for the resonance angle. The short circuit current between anode and cathode correlates the response of the detector towards propagating plasmon waves.

The plasmon detector was tested in an aqueous environment compatible with biosensing assays performed. To take the reflectivity and photocurrent data, the device was placed in a PDMS (Polydimethylsiloxane) microfluidic mold, held in place by mechanical pressure and biological buffers were flown above the device. In Fig. 4-3 reflectivity and photocurrent are plotted as a function of incident angle taken in

HEPES (4-(2-hydroxyethyl)-1-piperazineethanesulfonic acid) buffer.

Reflectivity dependence on incidence angle shows a decrease in reflectivity (black circles) around 58 degrees when plasmons are excited across the structure. At the same time a resonant peak is observed in the short circuit current of the photodiode (red circles). Numerical simulations are plotted with solid lines in black for current and red for reflectivity, however the resonance width for the experimental plots is larger than the theoretical prediction. While the refractive index and extinction coefficient were measured directly for the gold and the organic materials used, our model does not take into account the surface roughness of the device. Previous work demonstrated that the width of measured reflectivity curves is greater than the width calculated for a smooth surface.

4.3 Optimization of the near field plasmon detector

Standard surface plasmon resonance sensitivity is optimized by adjusting the metal thickness to an optimal value. For thick metal films most of the light is reflected instead of being absorbed by plasmon modes and for thin metal films the resonance width in increased.

We optimized the plasmon detector for metal contacts thicknesses that maximize sensitivity. The top contact which also functions as a protective layer from the aqueous environment was kept a thickness that preserves film continuity, 20 nm. In a numerical simulation, the bottom thickness of the anode was varied continuously and for each value the sensitivity of the device towards absorption of a 5 nm protein layer was calculated. In Fig. 4-4 we plotted the result of this simulation; sensitivity is maximized for a bottom layer gold thickness of about 27.5 nm.

In Fig. 4-5 we plot the performance of a surface plasmon resonance sensor in three cases: standard SPR that uses a single gold film of 50 nm (dotted line), a two near field plasmon detector of with optimized bottom metal contact thicknesses of gold

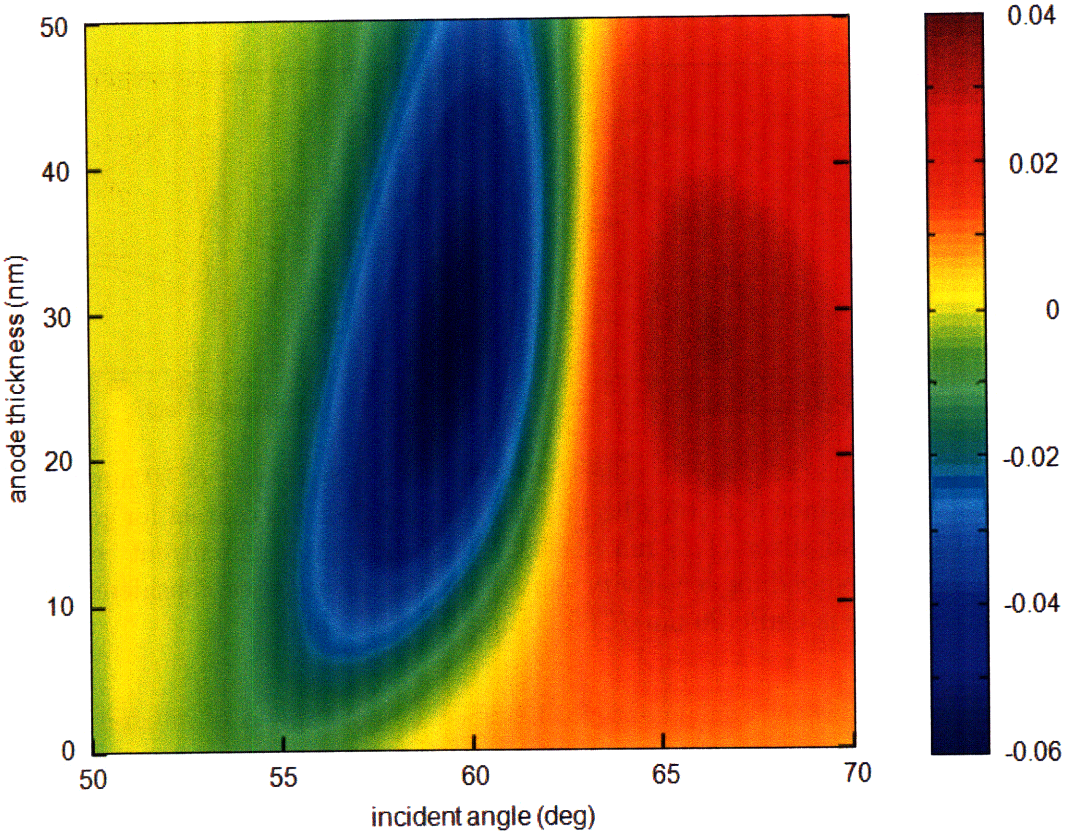

Figure 4-4: Optimization thickness of bottom Au cathode . The thickness of the top contact is kept constant at 20 nm. The maximum sensitivity is observed for 27.5 nm

(solid line, 27.5 nm) and silver (dashed line, 17.5 nm). In Fig. 4-5(a) reflectivity data is plotted in black and photocurrent data is plotted in red and in Fig. 4-5(b) we plot the sensitivity for all three devices measured as difference in signal after absorption of a 5 nm protein layer. In the near field detector cases considered the detector structure is 20 nm C60, 20 nm CuPc, 8.5 nm BCP. The use of silver for the bottom contact is motivated by the lower plasmonic losses in this material; a better performance is observed in both reflectivity and photocurrent data compared to a device that uses gold for both anode and cathode.

The reflectivity data allows for a direct comparison between standard SPR and our near field approach. The sensitivity of the single gold film is the highest, and the sensitivity of the best near field detector considered (silver bottom contact) is nearly half of that for standard SPR. Using a near field detector results in a loss of

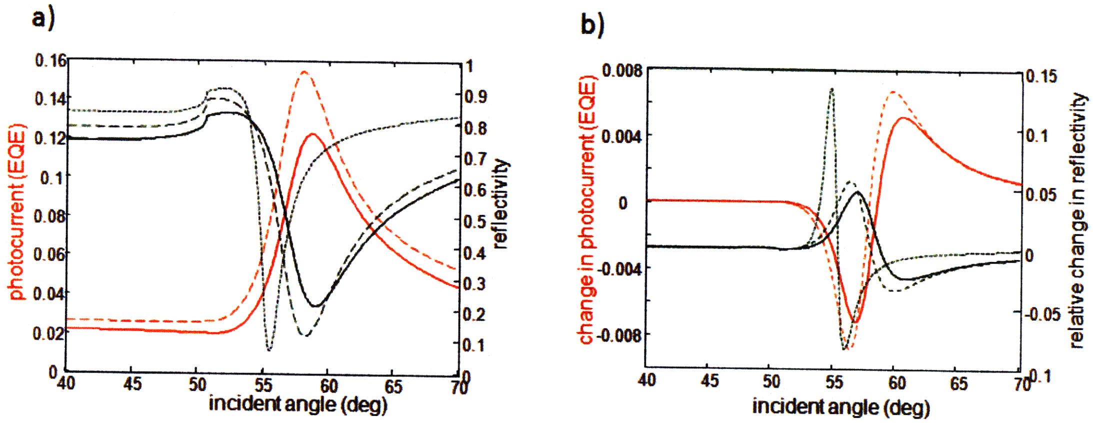

Figure 4-5: a) In black: plasmon reflectivity curves for a gold layer of 50 nm (dotted line), near field plasmon detector with optimal thickness bottom contact for gold (27.5 nm, solid line) and silver (17.5 nm, dashed line). In red: photocurrent resonance curves. b) Corresponding sensitivity curves for the three cases considered. The detector structure is CuPc(20 nm)/C60(20 nm)/BCP(8.5 nm)

performance, however it can potentially be offset by advantages of integration in a miniaturized solid state device.

4.4 Performace of the integrated OLED-near field plasmon resonance detector device

We estimated the performance of an integrated device using the angular mission OLED data (Fig. 4-2) and angular response of the near field plasmon detector (Fig. 4-3). The emission intensity profile for OLED devices that emit at different angles was approximated by shifting the measured OLED spectrum by a finite angular value. The overall photocurrent/reflectivity of integrated device was calculated by summing the reflectivity/photocurrent of the detector over all angles weighted by the magnitude of the angular emission of the OLED, which is normalized such that the numerical integral over all angles is unity.

An angle dependent response of the integrated device was calculated. This extrapolation allows prediction of the performance of the integrated device and direct comparison with both standard surface plasmon resonance, and the stand alone detector. While this approach has notable shortcomings, most notably not taking into account a varied angular outcoupled light intensity, it does provide a useful metric of evaluating the merit of integration.

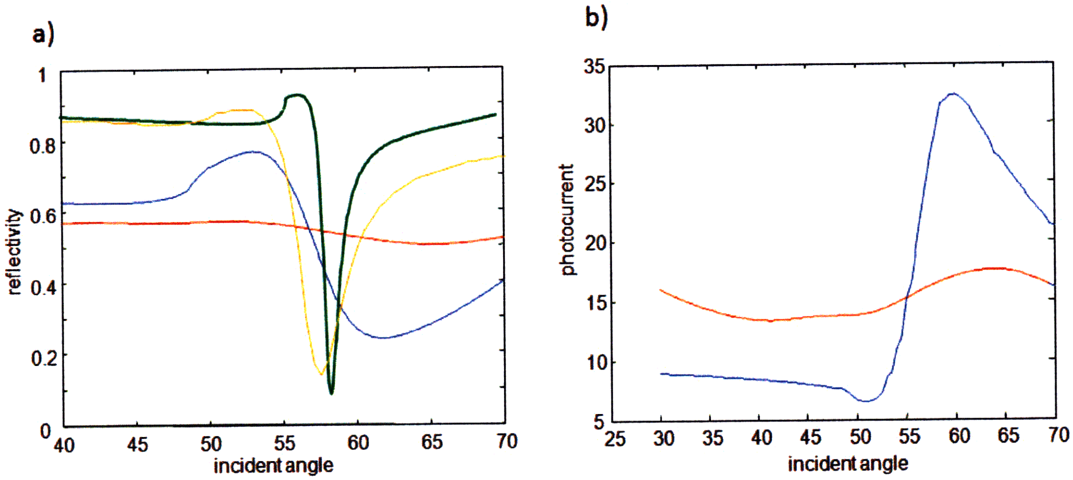

Figure 4-6: a) Reflectivity plots for 50nm gold film (green) (theory), 50 nm gold film (orange) (experiment), detector (20 nm Ag, 20 nm CuPc, 20 nm C60, 8.5 nm BCP, 20 nm Au) (experimental data, blue), integrated device (normalized OLED intensity and detector) (experimental data, red). b) Photocurrent plots for detector (experimental data, blue), integrated device (normalized OLED and detector, experimental data, red)

In Fig. 4-6(a) we plot the angular dependence of simulated reflectivity (green) for a 50 nm gold film, the experimentally measured reflectivity for a 50 nm gold film (orange), near field detector device (blue), and integrated OLED-near field detector device (red). Fig. 4-6(b) shows a photocurrent angular dependence plot of the near field detector and the integrated OLED-detector device. The plasmon resonances in reflectivity and photocurrent for the integrated device exhibit an increased width and decreased amplitude compared to the other cases considered, both of which decreasing the sensitivity.

4.5 Discussion

Miniaturization and integration of surface plasmon resonance sensors promise low cost, real time biodetection solution. In addition, an array of micro scale sensors can be fabricated on the same substrate to allow multiplexing of a battery of assays onto the same chip for multiple analyte screening in a single run. In this work we propose an integrated device consisting of a plasmon source and detector fabricated in a vertical structure on a high index substrate.

We demonstrated enhanced emission from a microcavity OLED at angles compatible with excitations of surface plasmons in the near field detector. The intensity maximum for angular emission was adjusted by varying the cavity length of the OLED. The near field detector response was characterized for both far field reflectivity and near field photocurrent as a function of incidence angle of incoming light.

Fabrication of the integrated device requires precise tuning of the OLED emission and good reproducibility of growth conditions. Its performance is decreased compared to the standard approach in surface plasmon resonance that measures the reflectivity of a gold film. The lower sensitivity is caused by a wider plasmon resonance in the near field detector compared to bare gold film. The fairly wide angular distribution of the OLED emission increases the overall wide resonance of the integrated device, resulting in quality factors significantly below the one for gold.

While the current sensor design has certain shortcomings with respect to sensitivity and stability they can be addressed by better surface functionality using a dextran hydrogel matrix, and improvements in the performance of the near field detector and OLED.

Chapter 5

Combinatorial detection of volatile organic compounds using metal-phthalocyanine field effect transistors

5.1 Abstract

We apply percolation theory to explain the operation of multiple-use gas sensors based on organic field effect transistors (OFETs). For reversible operation, we predict that energetic disorder in the channel can obscure interactions with the analyte, since chemically-induced traps are overwhelmed by the natural disorder. Consequently, the sensitivity of an energetically disordered OFET-based chemical sensor is significantly inferior to the ideal disorder-free case. Current modulation in disordered OFETs is predicted to rely on morphological alteration of percolation paths. The theory is compared to results from an array of metal phthalocyanine (MPC) transistors exposed to low concentrations of solvents. Despite the presence of very large adsorption fractions of solvent on the channel, the current modulation is small, consistent with theory. Chemical selectivity is possible, however, since the central metal atom of the MPC

determines the strength of the solvent-MPC interaction, which in turn determines the amount of solvent adsorbed on the OFET channel. This work suggests that OFET-based sensors may be better suited to applications where the analyte binding energy exceeds the intrinsic energetic disorder of the organic semiconductor.

5.2 Introduction

Organic semiconductors offer several advantages for chemical sensing applications[41, 23]. Conjugated molecules and polymers can be synthesized to combine chemical transduction and electronic transport functions, simplifying the design of a chemical sensor. Furthermore, for low cost applications, van der Waals bonded organic semiconductors can be economically deposited on a variety of substrates. For example, organic semiconductors may be deposited directly onto packaging materials to detect food spoilage. The archetype chemically-sensitive organic semiconductor is a thin film of metal phthalocyanines (MPCs). These films have been demonstrated to detect gases such as NO[32, 42], NO_2[38, 40, 39, 54], O_3[20, 21], Cl_2[18, 19] and volatile organic compounds (ethanol[64], tert-butylamine, methanol[47], hexane and ethyl acetate[65, 63, 57, 66, 59]). MPCs are extremely stable materials and are currently produced in quantities exceeding 80,000 tons annually for use in pigments[72]. In the solid state most MPCs stack, maximizing the orbital overlap of their extensively conjugated PC ligands[58, 37]. Consequently, the hole mobility in MPC films generally exceeds $\sim 10^{-3}$ cm^2/Vs, quite good for a van der Waals bonded material. When used in chemical sensors, analyte molecules typically bind to the central metal ion of the MPC, and chemical selectivity is obtained by varying this atom. In excess of fifteen MPCs are readily available, aiding in the fabrication of combinatorial arrays. In this work we examine the Cu^{2+}, Ni^{2+}, Co^{2+} and Zn^{2+} variants.

In general, the sensitivity of detection improves if analyte molecules react strongly with the sensor. However, this presents a tradeoff to sensor design since tightly bound analytes lengthen recovery times. For MPCs, analyte binding to the central metal ion is typically weak, suggesting that MPC based sensors are most suitable for low sensitivity but multiuse applications. For example, chemical sensing with MPCs is thought to be analogous to the olfactory system, another reusable sensor based on weak interactions with analytes. Indeed, it has been proposed that the olfactory system is also based upon coordination of analyte molecules to metal ions bound by olfactory receptor proteins[70].

Several strategies have been used to fabricate MPC based sensors. Optical sensors monitor changes in the wavelength dependent absorbance of metalloporphyrins[56] and MPCs[64] upon analyte binding. If an electrical output is desired, resistive sensors measure alterations in conductivity[49] upon exposure to gases. The number of free carriers in intrinsic MPC films is low, however, and chemiresistors require thicker films to improve the signal to noise ratio, at the cost of longer diffusion-limited response times.

In the present work we examine transistor based sensors which employ a gate electrode to attract charge carriers into a MPC film. While chemiresistors yield only one dimensional conductance modulation data, the larger set of transistor parameters allows better characterization and identification of gas interactions[68]. Two dimensional gate-induced charge accumulation in thin film transistors also enables the use of thin ($\sim$ 100Å) MPC films with faster response times due to rapid penetration and equilibration of gas molecules within the thin MPC channel.

In the next section of this chapter, we present a general theory of charge carrier mobility modulation in gas sensors based on organic field effect transistors (OFETs). There are two limits: when the interaction energy between the between organic semiconductors and analyte molecules is greater than the energetic disorder, trap formation yields large modulations in current. For materials with larger energetic disorder and weak interactions, the charge carrier mobility is primarily modulated by morphological changes, especially the modification of percolation pathways upon the intercalation of solvent molecules. Both the steady state and transient mobility modulation is dependent on solvent concentration and weakly dependent on the particular solvent employed.

Experimental results for an MPC transistor array are described in later sections.

We characterize the stability and solvent concentration dependence of charge carrier mobility modulations in MPC thin film transistors. Transient and steady state channel currents are analyzed to discriminate between the solvents acetonitrile, tetrahydrofuran and toluene. The predictions of the theory section for disordered OFETs are confirmed for the MPC system. Finally, we discuss the prospects for MPC-based chemical sensors in the last part and conclude.

5.3 Theory

In this section we develop the theory of vapor interaction with the OFET channel. We analyze both steady state and transient modulation in the channel current.

5.3.1 Steady state analysis

Similar to other polycrystalline organic semiconductors[67], charge transport in the MPC-based OFET channel is dominated by traps. Consistent with direct measurements of the trap population in organic semiconductors, the traps are modeled by an exponential distribution:

$$g(\epsilon) = \frac{N_0}{E_T} \exp\left(\frac{\epsilon}{E_T}\right), \quad (-\infty < \epsilon \leq 0), \tag{5.1}$$

where ϵ is the energy of the state, N_0 is the total number of states, and E_T is the characteristic trap energy. The traps are deep, i.e. $E_T >> kT$, where k is Boltzmann's constant and T is temperature.

The other key parameter for organic semiconductor-based chemical sensors is the binding energy, E_B, of the analyte-organic semiconductor interaction. For MPC transistors, we assume that solvent-MPC interactions rigidly shift MPC site energies by E_B, where E_B is negative for attractive interactions. There are two limits, $|E_B| \gg E_T$ and $|E_B| \ll E_T$, described here as the strong and weak interaction limits, respectively.

The strong interaction limit ($|E_B| \gg E_T$)

In this limit the binding energy of solvent-MPC interactions is much larger than the width of the density of charge transport states. Thus we model the intrinsic and chemically modified MPC sites by two discrete energy levels: a charge transport level with charge carrier mobility μ_0, and a trap level containing immobilized charge carriers. Following conventional trap charge limited transport theory we find that the effective charge carrier mobility is:

$$\mu = \mu_0 \frac{1}{1 + \frac{f}{1-f} \exp[-E_B/kT]}, \tag{5.2}$$

where f is the fraction of MPC molecules with an adsorbed solvent molecule. In the limit that $f$is small, we get:

$$\frac{\Delta I}{I} = -f \exp[-E_B/kT]. \tag{5.3}$$

Defining a sensitivity, S, normalized to the channel current we get:

$$S = \frac{1}{I} \frac{d\Delta I}{dc} = -\exp[-E_B/kT]. \tag{5.4}$$

Thus, the sensitivity depends exponentially on the binding energy of analyte interactions, enabling discrimination. In organic semiconductors, however, energetic disorder is typically significant, (i.e. $E_T \gg kT$). Hence the strong interaction limit is often associated with irreversible organic transistor-based sensors. The combination of large current modulation and reversibility is possible, however, in highly ordered channels: $ET \ll kT$.

The weak interaction limit ($|E_B| \ll E_T$)

The conductivity of the trap filled film may be modeled as percolation problem in which the system is approximated by a network of connected clusters. A cluster is defined such that the conductive path between any two sites is higher than a critical cutoff conductivity. As the limiting conductivity is decreased, the overall size of the clusters increases until it diverges (one infinite cluster is formed) and the conductivity is dominated by the cutoff value. The cluster is treated as infinite when each constituent molecular site is linked to a critical number, B_C, of neighboring molecules. Previous numerical simulations suggest that $B_C = 2.8$ in three dimensional disordered materials. Since deep trap sites have fewer neighboring states of similar energy, applying bias to the gate modulates mobility by filling the deepest, most isolated traps. As higher energy trap states are populated the conductivity increases dramatically. The charge carrier mobility obtained from this analysis is[69]:

$$I \sim V_D \left[\frac{1}{\alpha^3 B_C} (C_g V_{gs})^2 \right]^{E_T/kT}, \tag{5.5}$$

where V_{gs} is the gate bias relative to the source potential, and C_g is the gate-channel capacitance and a is an inverse length that characterizes the spatial tunneling probability rate[** cite 29].

On exposure to gas, two effects are possible: the energy of the trap states may be modulated, or the intercalation of gas molecules within the film may physically change links in the percolation pathways. We consider each of these effects in turn.

Solvent modulation of trap energies

Again, we assume that solvent-MPC interactions rigidly shift MPC site energies by E_B, where E_B is negative for attractive interactions. Hence, as a function of the adsorbed solvent fraction, f, the density of states is:

$$g(\epsilon) = \frac{N_0}{E_T} \exp\left(\frac{\epsilon}{E_T}\right) \left(1 - f\left(1 - \exp\left(\frac{E_B}{E_T}\right)\right)\right), \quad (-\infty < \epsilon \le E_B). \tag{5.6}$$

We can safely ignore states in the energy range $E_B < \epsilon < 0$ in the weak interaction regime, (i.e. the Fermi energy, $E_F \gg |E_B|$).

Under the weak interaction limit, Eq. 5.6 may be further reduced to

$$g(\epsilon) = \frac{N_0(1 - fE_B/E_T)}{E_T} \exp\left(\frac{\epsilon}{E_T}\right), \quad (-\infty < \epsilon \leq E_B). \tag{5.7}$$

In both Eqns. 5.6 Eq. 5.7 and the shape of the density of states is unchanged by solvent interactions. Under the model of Eq. 5.5, the charge carrier mobility depends only on the characteristic trap energy, E_T, and the density of charge carriers, both of which are unchanged in the presence of solvents. Hence solvent modulation of trap energies does not affect mobility in the weak binding limit.

Solvent intercalation and morphological modulation of percolation pathways

Numerical simulations of the CuPC, CoPC, NiPC and ZnPC show that solvents bind to the central metal ion in an MPC, thereby disrupting $\pi - \pi$ stacking. A representative result is shown in Fig. 5-1(a) for CoPC bound to acetonitrile. If every solvent molecule changes a link between MPC sites then the effective tunneling decay constant is altered as:

$$\alpha_{eff} = \alpha + f\Delta\alpha \tag{5.8}$$

where α_{eff} is the effective tunneling decay constant and $Delta\alpha$ is the change in tunneling decay upon intercalation of a solvent molecule. If f is small ($f \ll 1$), the solvent-dependent change in charge carrier mobility is

$$\frac{\Delta I}{I} = -3f\frac{E_T}{kT}\frac{\Delta\alpha}{\alpha}. \tag{5.9}$$

The normalized sensitivity is

$$S = \frac{1}{I}\frac{d\Delta I}{df} = -3\frac{E_T}{kT}\frac{\Delta\alpha}{\alpha}. \tag{5.10}$$

Previous work found that solvent induced phase transitions in organic films cause changes in inter-planar distances of 2.5-6%[27] and it is likely that the relative variation in α is of the same order. $\Delta\alpha$ is expected to introduce some chemical selectivity, but the dependence is not exponential, as in the strong interaction limit. Thus, the relative change in channel current is small and the sensitivity and selectivity of the steady-state channel current is low relative to the ordered channel case.

Transient analysis

The fraction, f, of MPC sites with an adsorbed solvent molecule varies depending on the strength of chemical interactions. Assuming that the MPC film is uniform, the adsorbed solvent molecules do not interact, and that the adsorbed solvent forms at most a monolayer, we describe the dynamics using the Langmuir model:

$$MPC + S \underset{k_{-1}}{\overset{k_1}{\longleftrightarrow}} MPCS \tag{5.11}$$

where MPC is a generic metalo-phthalocyanine, S a solvent molecule, MPCS the solvent bound MPC complex, and k_1 and k_{-1} the forward and backward rates, respectively. The fraction of MPCS is given by:

$$f(t) = f_M \frac{k_1 c_0}{k_1 c_0 + k_{-1}} \left(1 - e^{-(k_1 c_0 + k_{-1})t}\right) + f(0) e^{-(k_1 c_0 + k_{-1})t} \tag{5.12}$$

where $f(0)$ is the initial solvent fraction adsorbed on the film, c_0 is the solvent concentration in ambient, and f_M is the saturation adsorption fraction, corresponding to the formation of a complete monolayer of adsorbed molecules. This constant takes into account the possibility that not all MPC molecules are at the surface. From Eq. 5.12 , the rates of change in $f(t)$ for step function modulation of solvent ambient concentration are $k_{ON} = k_1 c_0 + k_{-1}$, and $k_{OFF} = k_{-1}$. Rearranging, the steady state fraction, f, of sites with solvent adsorption is

$$f = f_M(1 - k_{OFF}/k_{ON}). \tag{5.13}$$

Thus, we can extract the fraction of sites with adsorbed solvent from the transient response. The steady state fraction of MPC sites with an adsorbed solvent molecule is given by the Langmuir isotherm:

$$\frac{f}{f_M} = \frac{1}{1 + a/c_0} \tag{5.14}$$

where a is a constant having units of concentration that equals k_{-1}/k_1 and is dependent on the binding energy of solvent-MPC interactions; a is treated as a fit parameter in this work. In the limit of low environmental concentrations ($c_0 \ll a$) the change in current is linear with the concentration of the analyte, while as the concentration increases, the current drop reaches a concentration independent limit.

5.4 Experimental results

In this section we investigate the sensing characteristics of thin film MPC transistors in the presence of common solvents. The devices were fabricated in the back gate geometry, using a p doped silicon substrate with 100 nm thick thermal oxide, 10 nm thick MPC films were deposited by thermal evaporation under vacuum (10^{-6} torr), followed by deposition of 3-nm-thick Cr and 50-nm-thick Au contacts through a shadow mask; see Fig. 5-1(c). The width and length of the channel were W = 2 mm and L = 50 m, respectively. The transistors conduct holes in the on state, and the mobility as extracted from the saturation region of the current voltage characteristics is on the order of 3×10^{-4} cm^2/Vs. Solvent testing was performed in a sealed chamber and the solvent concentration was controlled using two mass flow controllers: one regulating the flow of nitrogen through a bubbler filled with the volatile compound to be analyzed, and the other controlling a pure nitrogen stream used to dilute the solvent. The final solvent concentrations were calculated using Antoine's equation assuming that the nitrogen is saturated as it passes through the bubbler.

Geometry optimizations were performed using HyperChem v. 7.0 software package (available from HyperCube) using the PM3 semi-empirical basis set. The parameters

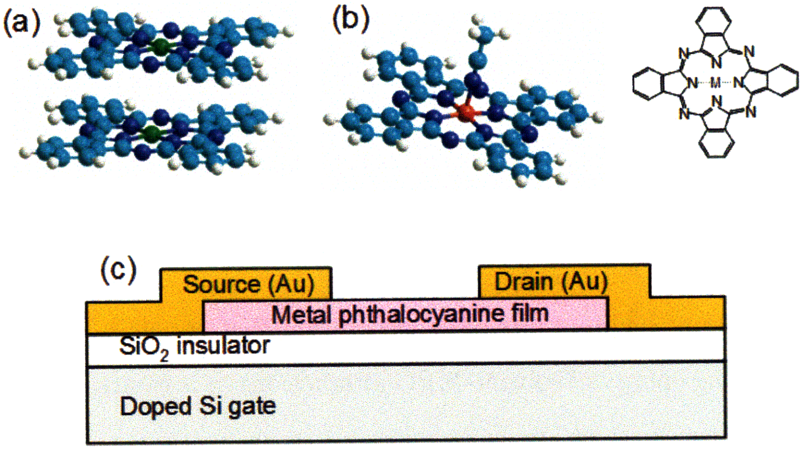

Figure 5-1: (a) Numerical simulations for the geometry optimization of copper phthalocyanine when stacked in a thin film. (b) Simulations of cobalt phthalocyanine in the presence of the solvent molecule acetonitrile. The solvent intercalation breaks the stacking of neighboring MPC molecules and effectively breaks a percolation pathway between the MPC sites. (c) The structure of the field effect transistor-based sensors studied in this work. A 10-nm-thick layer of metal-phthalocyanine (see inset) was deposited on a p-boron doped silicon wafer with 100-nm-thick thermal oxide. Gold source and drain contacts are patterned on top of the organic.

used for optimizing the geometries of these molecules (shown in Fig. 5-1): total charge = 0, spin multiplicity = 1 ($s = \frac{1}{2}$ for copper phthalocyanine dimer - Fig. 5-1(a)) or 2 (s = 1 for cobalt phthalocyanine interaction with acetonitrile - Fig. 5-1(b)), spin pairing = unrestricted Hartree-Fock, and using the Polak-Ribiere conjugate gradient algorithm for energy minimization determination (RMS gradient = 1×10^{-8} kcal/(Å$\cdot$ mol), *in vacuo*).

Representative current-voltage characteristics (I_{ds} vs. V_{ds} and I_{ds} vs. V_g) under nitrogen or 500 ppm ethanol are shown in Fig. 5-2 for a MPC transistor. The data shows a decrease in channel current at all sampled points, while no significant change in the threshold voltage is observed.

The stability of the same transistor is shown in Fig. 5-3(a). Because the channel current decreases gradually with time, perhaps due to the filling of deep traps, the gate bias was pulsed in periods of 5 s. It was applied for 100 ms, and then removed for 4.9 s to allow de-trapping, yielding a fairly stable current baseline. To obtain the transient rates k_{ON} and k_{OFF}, channel current modulation was fitted with a double

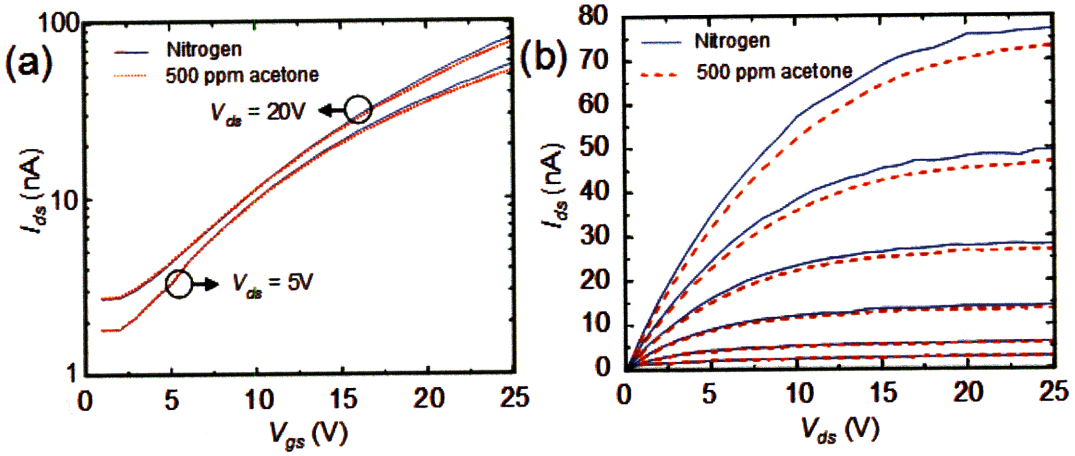

Figure 5-2: (a) I_{ds} vs. V_{gs} for V_{ds} -5 and -20 V and (b) I_{ds} vs. V_{ds} characteristics taken at Vgs = 0, -5, -10, -15, -20, -25 V for a ZnPc transistor. Solid lines represent data taken in a nitrogen atmosphere, and dotted lines data taken in 500 ppm acetone in nitrogen. Exposure to solvent decreases the conductivity of the channel but does not significantly influence the threshold voltage.

exponential function to correct for baseline changes. The fast solvent-on transient is assumed to be diffusion limited. In contrast, the recovery of the channel current when the solvent is flushed from ambient is typically much slower since solvent molecules are bound, albeit weakly, to MPC molecules. Both solvent-on and solvent-off transients may include diffusion through the film.

The solvent concentration dependence of the channel current modulation is shown in Fig. 5-3(b) for the representative ZnPC-Toluene combination. Solvent was introduced at concentrations between 100 ppm and 400 ppm in increments of 100 ppm. The channel current is observed to vary sub-linearly with increasing concentration, consistent with Eq. 5.14.

In Fig. 5-4(a) we summarize the steady state current modulation ΔI/I and transient measurements of k_{OFF} and k_{ON}. The transistor array includes ZnPC, NiPC, CoPC and CuPC transistors at drain source voltage of -20V and gate bias -20V. Each device is exposed to 100 ppm of either acetonitrile, toluene or tetrahydrofuran. The

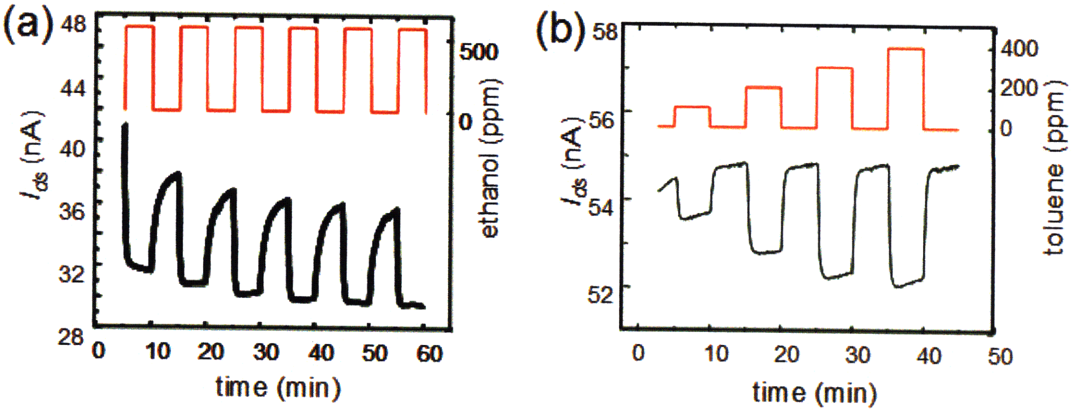

Figure 5-3: (a) The transient responses of ZnPC-based sensors were obtained by modulating the solvent concentration. Here, in a representative test of the stability of ZnPC sensors, we show the channel current modulation in a ZnPC sensor is exposed to 500 ppm ethanol (V_{gs} = -20V, V_{ds} = -20V). To minimize the charging of deep traps in the channel the gate voltage was applied for 100 ms, the channel current measured, and then the gate returned to zero bias for 4.9 s to allow de-trapping. After about 30 min the drain current is observed to stabilize although a slow decrease in channel current remains. (b) The linearity of MPC sensors is tested by modulating the solvent concentration. A representative result is shown here for a ZnPC sensor exposed to varying concentrations of toluene. The current modulation is observed to vary approximately linearly at low solvent concentration.

MPC arrays yield a characteristic fingerprint for each solvent, demonstrating that the current modulation yields chemically selective data. The modulation is small, but consistent with the model of Eq. 5.9.

The transient data enables us to separate out potential sources of chemical selectivity. In particular, the relation between the ON and OFF transients reveals the strength of solvent-channel interactions; solvent is bound tightly to the channel when $k_{ON} \gg k_{OFF}$. Comparing Fig. 5-4(a) and (b), we observe that the transient data reflects the broad trends of the current modulation data. We can divide the MPC-solvent interactions into two groups. The stronger interactions with $k_{ON} \gg k_{OFF}$ include the MPC-acetonitrile combinations, and CoPC and NiPC with toluene. These

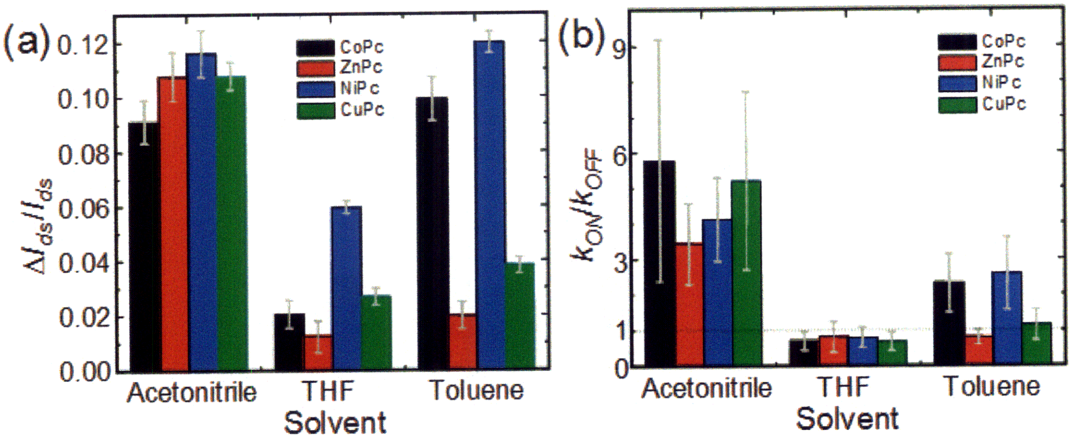

Figure 5-4: (a) The steady state current modulation data $\Delta I_{ds}/I_{ds}$ and (b), the ratio of transient rates k_{ON}/k_{OFF} upon exposure to 100 ppm of the specified solvents. Combinatorial analysis yields unique 'fingerprints' for each solvent. Transistor bias conditions are V_{ds} = -20V, V_{gs} = -20V.

combinations also exhibit the largest channel current modulation. The weaker interactions include the MPC-THF combinations, and CuPC and ZnPC with toluene. The broad correlation between Fig. 5-4(a) and (b) suggests that the chemical selectivity observed in Fig. 5-4(a) is principally due to binding-energy-dependent variations in the fraction of MPC sites with solvent adsorption, i.e. a given MPC transistor adsorbs different surface densities of each solvent.

We focus on the strongly interacting MPC-solvent pairs in Fig. 5-5. We fit the concentration dependencies to Eq. 5.14. Interestingly, all the strongly interacting MPC-solvent pairs can be fit with the same binding-energy-dependent constant, a = 80 ppm. Rather, the chemical selectivity within this set appears to be dominated by morphological factors: $\Delta\alpha$ - the morphological change on solvent adsorption, and f_M - the saturation adsorption fraction, which depends on the channel surface area. Note that in most cases, the adsorption fraction approaches saturation. Thus, the maximum possible current modulation in these transistors appears to be only ~ 10-20%.

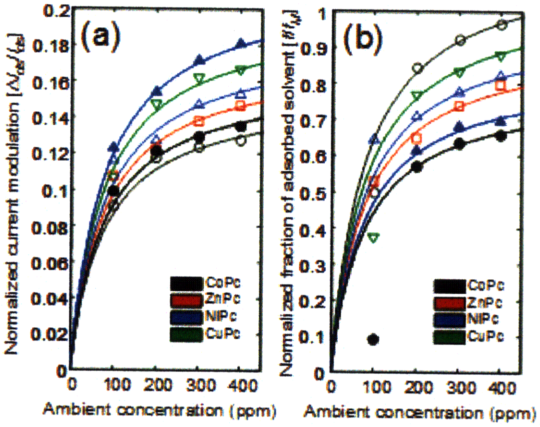

Figure 5-5: (a) The concentration dependence of the steady state current modulation data $\Delta Ids/Ids$ for strongly interacting solvent-MPC pairs. (b) The concentration dependence of the normalized fraction of adsorbed solvent for the same pairs as calculated from the transient data. In both (a) and (b) the lines are fits to Eq. 5.14 with a = 80 ppm and normalization constant +/- 20%. Solid symbols correspond to toluene and empty symbols to acetonitrile. Circles are CoPC, squares ZnPC, upward triangles NiPC and downward triangles are CuPC. Note that the weaker interactions are not well described by the simple kinetic model since the Langmuir isotherm requires $k_{ON}/k_{OFF} > 1$. Although this conclusion is tempered by the lower signal to noise and more unstable steady state response in the weakly interacting combinations.

5.5 Conclusion

This work presents a general theoretical description of the impact of weakly bound solvents in disordered semiconductors ($E_B \ll E_T$). The steady state current modulation yields a characteristic response for each solvent dependent on the solvent adsorption on the channel. Transient data may be used to specifically probe the ratio of the channel adsorption fraction to the ambient concentration. Despite the presence of adsorption fractions that approach saturation, the observed current modulation is $< 20\%$ and comparable to the channel current drift. We conclude that the magnitude of the channel current modulation yields relatively poor sensitivity since the tail of the density of states obscures the effect of solvent induced traps. Rather, the solvent breaks percolation pathways via intercalation and disruption of $\pi - \pi$ interactions between neighboring molecules. In contrast with the relatively poor performance observed in transistors with energetically disordered channels, we predict an exponential increase in sensitivity for energetically-ordered materials. We also find that differing adsorption of solvent on the channel is the principal determinant of chemical selectivity, which adversely affects selectivity in cases where the adsorption fraction approaches saturation. The model of sensitivity and selectivity is supported by numerical simulations of MPC-solvent interactions, a sub-linear dependence of channel current modulation on solvent concentration, and the consistent decrease in mobility for all solvent MPC pairs tested.

Finally, we discuss the implications of the theory and results for combinatorial organic transistor-based sensors. Combinatorial array systems, also known as e-noses, use multiple sensing elements and, although no single element is specific to the volatile organic compound, the response of the whole array provides a unique identification pattern for the analyzed species[33].

There are two disadvantages associated with reusable combinatorial arrays. First, reducing the binding energy between sensor and analyte such that the sensor is reusable inevitably reduces the sensitivity. Second, interpreting the output of reusable array sensors becomes increasingly difficult, and even impossible, when multiple analytes are present. Both of these disadvantages motivate the use of organic transistor-based sensors in simple applications where the sensitivity demands are relaxed and the economical fabrication of organic devices can be exploited.

On the other hand, the main advantage of array sensors resides in the fact that there is no need to design chemical specificity, making weakly interacting species such as solvents easier to detect. In addition, because array sensors do not rely on strong covalent interactions, but rather on much lower energy interactions, the recovery time of the sensor is greatly improved.

Chapter 6

Conclusion

Organic semiconductor devices used in commercial applications face two main challenges: yield and lifetime. Both problems can be addressed by use of more robust materials, device architecture, and packaging in an inert environment. During completion of the research projects both challenges were exacerbated by more stringent processing: immersion in solvents for functional specificity, and operation in aqueous solution. Among advantages over other organic devices most notable are short operation time of only a few hours (orders of magnitude less than the lifetime requirement for an organic light emitting diode used in display applications) and small device length scale (since yield in generally inversely proportional with size). The surface plasmon detector can be improved in almost every aspect: lower refractive index materials for the photovoltaic, less lossy metals for the plasmon waveguide, improved functionalization with carboxy-methyl-dextran for a more efficient overlap between the plasmon field and binding region, and a more robust processing that increases the yield. In addition it is critical to perform a systematic evaluation of the sources of noise in the sensor as the resolution of the method is defined as three times the noise level. For instance it is important to understand if and to what extent the organic semiconductor detector is noisier than far field detectors used in surface plasmon resonance instrumentation: charge coupled device and diode array detectors. The same argument holds for performance comparison between the organic light emitting diode and the current light sources used in traditional SPR sensors.

The numerical simulation for sensitivity of the partially optimized plasmon detector falls only within a factor of two of typical SPR devices, therefore we do not see it as an impediment toward finding a commercial use for the near field sensors. Instead, the main obstacle seems to be the ability of the devices to operate after functionalization, especially considering that the industry processing is considerably more stringent than the one we used. For user convenience it is expected that an SPR sensor is fully operational and ready for immediate use, hence functionalization has to be done prior to packaging. Based on our experience the two main factors that affected the yield are layers morphology and damaging through surface tension upon immersion in liquids since adhesion between metals and organics is generally poor.

The utility of organic thin film transistors as sensors is limited by their low sensitivity and low specificity. The maximum change in transistor current during operation is around 10-20% under conditions that saturate the binding sites within the organic film. In addition, under continuous measurement the source drain current decreases in time due to filling a deeper trap states. This poses a challenge to the stability and referencing of the base line. The semiconductor materials that we used (metal phthalocyanines) do not possess intrinsic specificity towards the detected analytes so a single transistor can not uniquely identify molecular species. Instead of a single device we used an array of transitors to probe interaction of anlytes, however the main challenge is that the responses of the individual elements are not orthogonal.

The main accomplishments of the work presented in this work are chemical detection with an array of organic devices and miniaturized architecture for a surface plasmon resonance biosensor. When analyzing sensors based on organic semiconductor devices one has to reconcile two conflicting trends. On one hand organic devices have poor stability and require substantial efforts for packaging; on the other hand the intrinsic operation of a sensor requires exposure to degradation agents, sometime the same exact species that are measured.

Appendix A

Numerical simulations for calculating relectivity, photocurrent and electric field amplitude in the plasmon detector

This appendix presents a Matlab code that calculates the reflectivity, photocurrent and electric field in an arbitrary dielectric stack, numerical data used in the chapters 'Near Feld detector for integrated surface plasmon resonance biosensor applications' and 'Integrated surface plasmon resonance biosensor based on organic semiconductor devices'. It assumes plane waves monochromatic light of wavelength 670 nm, that coincided with the wavelength of the solid state laser used in the experimental setup. The dielectric layers are defined as a one dimensional stack of thickness t and dielectric constant ϵ. The dielectric constants of various organic and inorganic materials were calulated from the n and k values aquired with an Aquila nkd-8000 thin film measurement instrument. The code requires input of material files that contain n and k values for the 401-795 nm wavelength range.

```
% Finds the photocurrent, reflectivity and electric field of a multilayer dielectric stack
% Valid only for plane waves, not dipole or near fied
clf
clear
h=6.62e-34;
q=1.6e-19;
light=3e8;
PV=3; % PV layer number (initial one)
res=100; % resolution of the E field, res # E points in one layer
% dielectric constant data first row is wavelength data (in nm) second row is dielectric constants
ITO = [200 250 300 350 400 450 500 550 600 650 700 750 800 850 900; 2.6000+i*2.8800
4.3500+i*3.0800 5.6700+i*1.4400 4.6176+i*0.3010 3.9996+i*0.0800 3.6099+i*0.0380
3.4224+i*0.0370 3.2399+i*0.0360 3.1683+i*0.0356 3.0624+i*0.0350 2.9928+i*0.0346
2.8899+i*0.0340 2.8222+i*0.0504 2.7554+i*0.0498 2.6567+i*0.0489];
ag_nk=load(’ag.nk’); ag = [ag_nk(:,1)’; ag_nk(:,2)’.^2-ag_nk(:,3)’.^2+2*i*ag_nk(:,2)’.*ag_nk(:,3)’];
au_nk=load(’au.dat’); au = [au_nk(:,1)’; au_nk(:,2)’.^2-au_nk(:,3)’.^2+2*i*au_nk(:,2)’.*au_nk(:,3)’];
bcpag_nk=load(’bcpag.nk’); bcpag = [bcpag_nk(:,1)’;
bcpag_nk(:,2)’.^2-bcpag_nk(:,3)’.^2+2*i*bcpag_nk(:,2)’.*bcpag_nk(:,3)’];
bcpau_nk=load(’au_bcp.dat’); bcpau = [bcpau_nk(:,1)’;
bcpau_nk(:,2)’.^2-bcpau_nk(:,3)’.^2+2*i*bcpau_nk(:,2)’.*bcpau_nk(:,3)’];
cupc_nk=load(’cupc.nk’); cupc = [cupc_nk(:,1)’;
cupc_nk(:,2)’.^2-cupc_nk(:,3)’.^2+2*i*cupc_nk(:,2)’.*cupc_nk(:,3)’];
c60_nk=load(’c60.nk’); c60 = [c60_nk(:,1)’;
c60_nk(:,2)’.^2-c60_nk(:,3)’.^2+2*i*c60_nk(:,2)’.*c60_nk(:,3)’];
bcp_nk=load(’bcp_r.dat’); bcp = [bcp_nk(:,1)’;
bcp_nk(:,2)’.^2-bcp_nk(:,3)’.^2+2*i*bcp_nk(:,2)’.*bcp_nk(:,3)’];
ptcbi_nk=load(’ptcbi.dat’); ptcbi = [ptcbi_nk(:,1)’;
ptcbi_nk(:,2)’.^2-ptcbi_nk(:,3)’.^2+2*i*ptcbi_nk(:,2)’.*ptcbi_nk(:,3)’];
mg_nk=load(’Mg_palik.nk’); mg = [mg_nk(:,1)’;
mg_nk(:,2)’.^2-mg_nk(:,3)’.^2+2*i*mg_nk(:,2)’.*mg_nk(:,3)’];
```

```
alq3_nk =dlmread(’alq3_literature.dat’,’,’,0,0); alq3 = [0.1*alq3_nk(:,1)’;
alq3_nk(:,2)’.ˆ2-alq3_nk(:,3)’.ˆ2+2*i*alq3_nk(:,2)’.*alq3_nk(:,3)’];
tpd=bcp;
water = [200 1920; 1.33ˆ2 1.33ˆ2];
glass = [200 1920; 1.75ˆ2 1.75ˆ2];
medium = [200 1920; 1.46ˆ2 1.46ˆ2];
air = [200 1920; 1ˆ2 1ˆ2];
%clear ag; ag=glass;
% specify device structure
thickness=[400e-10 200e-10 200e-10 200e-10 85e-10 200e-10 515e-10];
L_d=70e-10; L_a=100e-10; % L_a is c60d
N=max(size(thickness))+2;
% specify wavelength range
dlambda=4; % in nm
wavelength_array=670;%[401:dlambda:795]; % in nanometers
% specify angle range
theta_array=[45:0.1:65]*pi/180; %pi/2*[0:0.01:0.90];
for l=[1:max(size(wavelength_array))],
wavelength=wavelength_array(l);
% incoming_charge(l)=interp1(sun(1,:),sun(2,:),wavelength)/h/light*wavelength*1e-9*q; %
Amount of charge generated if all light absorbed
end
% norm_sun=incoming_charge/sum(incoming_charge,2); % per meter square
for l=[1:max(size(wavelength_array))],
wavelength=wavelength_array(l);
% device structure
epsilon(1)=interp1(glass(1,:),glass(2,:),wavelength);
epsilon(2)=interp1(glass(1,:),glass(2,:),wavelength);
epsilon(3)=interp1(ag(1,:),ag(2,:),wavelength);
epsilon(4)=interp1(cupc(1,:),cupc(2,:),wavelength);
```

```
epsilon(5)=interp1(c60(1,:),c60(2,:),wavelength);
epsilon(6)=interp1(bcp(1,:),bcp(2,:),wavelength);
epsilon(7)=interp1(au(1,:),au(2,:),wavelength);
epsilon(8)=interp1(water(1,:),water(2,:),wavelength);
epsilon(9)=interp1(water(1,:),water(2,:),wavelength);
z0=[0 cumsum(thickness)];
k0=2*pi/wavelength/1e-9; nk0=sqrt(epsilon);
for p=[1:max(size(theta_array))],
theta=theta_array(p);
kz=sqrt(epsilon*k0^2-epsilon(1)*(k0*sin(theta))^2);
for j=[1:N-1],
r_te(j)=(kz(j)-kz(j+1))/(kz(j)+kz(j+1)); t_te(j)=2*kz(j)/(kz(j)+kz(j+1));
r_tm(j)=(epsilon(j+1)*kz(j)-epsilon(j)*kz(j+1))/(epsilon(j+1)*kz(j)+epsilon(j)*kz(j+1));
t_tm(j)=2*epsilon(j+1)*kz(j)/(epsilon(j+1)*kz(j)+epsilon(j)*kz(j+1));
A_te(:,:,j)=[1/t_te(j) r_te(j)/t_te(j) ; r_te(j)/t_te(j) 1/t_te(j)];
A_tm(:,:,j)=[1/t_tm(j) r_tm(j)/t_tm(j) ; r_tm(j)/t_tm(j) 1/t_tm(j)];
if j>1
L(:,:,j)=[exp(-i.*(kz(j)*(z0(j)-z0(j-1)))) 0 ; 0 exp(i.*(kz(j)*(z0(j)-z0(j-1))))];
end
% calculate overall prop matrix:
if j==1
S_te=A_te(:,:,j); S_tm=A_tm(:,:,j);
elseif j>1
S_te=S_te*L(:,:,j)*A_te(:,:,j); S_tm=S_tm*L(:,:,j)*A_tm(:,:,j);
end
end
E_te_l=[1 ; S_te(2,1)/S_te(1,1)] ; E_tm_l=[1 ; S_tm(2,1)/S_tm(1,1)];
E_te_r=[1/S_te(1,1); 0] ; E_tm_r=[1/S_tm(1,1); 0];
for j=N-1:-1:1
if j==N-1
```

```
E_te(:,j)=A_te(:,:,j)*E_te_r; E_tm(:,j)=A_tm(:,:,j)*E_tm_r; % calculated E is to right of the layer,
left of the interface
te=E_te(:,j); tm=E_tm(:,j);
elseif j<N-1
E_te(:,j)=A_te(:,:,j)*L(:,:,j+1)*te; E_tm(:,j)=A_tm(:,:,j)*L(:,:,j+1)*tm;
te=E_te(:,j); tm=E_tm(:,j);
end
Sz_te(j,p)=real(conj(kz(j))/kz(1)*(abs(E_te(1,j))^2-abs(E_te(2,j))^2+E_te(2,j)*conj(E_te(1,j))-
E_te(1,j)*conj(E_te(2,j))));
Sz_tm(j,p)=real(epsilon(1)/epsilon(j)*kz(j)/kz(1)*(abs(E_tm(1,j))^2-abs(E_tm(2,j))^2-
E_tm(2,j)*conj(E_tm(1,j))+E_tm(1,j)*conj(E_tm(2,j)))); % E_tm is actually magnetic field for TM
case
if j<N-1
if (Sz_te(j,p)-Sz_te(j+1,p))<-0.0001
display('energy conservation failure TE');
end
if (Sz_tm(j,p)-Sz_tm(j+1,p))<-0.0001
display('energy conservation failure TM');
end
end
end
Sz_te(N,p)=real(kz(N)/kz(1))*(abs(E_te_r(1))^2-abs(E_te_r(2))^2);
Sz_tm(N,p)=real(epsilon(1)/epsilon(N)*kz(N)/kz(1))*(abs(E_tm_r(1))^2-abs(E_tm_r(2))^2);
% Finding the field,absorption everywhere
for j=1:N-2
for jz=1:res
dx=thickness/res; nk(1,(j-1)*res+jz)=nk0(j+1);
Z((j-1)*res+jz)=z0(j)+dx(j)*jz;
E__te(:,(j-1)*res+jz)=(L(:,:,j+1)*E_te(:,j+1)).*[exp(i.*(kz(j+1)*dx(j)*jz));exp(-
i.*(kz(j+1)*dx(j)*jz))];
```

```
E__tm(:,(j-1)*res+jz)=(L(:,:,j+1)*E_tm(:,j+1)).*[exp(i.*(kz(j+1)*dx(j)*jz));exp(-i.*(kz(j+1)*dx(j)*jz))];
k_z_te((j-1)*res+jz) = conj(kz(j+1))/kz(1); k_z_tm((j-1)*res+jz) = kz(j+1)/kz(1);
epsilon_z((j-1)*res+jz) = epsilon(1)/epsilon(j+1);
end
end
E_tm_theta_z(p,:) = abs(E__tm(1,:)+E__tm(2,:)); E_te_theta_z(p,:) = abs(E__te(1,:)+E__te(2,:));
%Sz(l,:) = real(k_z_te.*(abs(E__te(1,:)).^2-abs(E__te(2,:)).^2+E__te(2,:).*conj(E__te(1,:))-E__te(1,:).*conj(E__te(2,:))));
Sz(l,:) = real(epsilon_z.*k_z_tm.*(abs(E__tm(1,:)).^2-abs(E__tm(2,:)).^2-E__tm(2,:).*conj(E__tm(1,:))+E__tm(1,:).*conj(E__tm(2,:))));
Sz_p(p,:) = Sz(l,:);
Abs(l,:) = -diff([Sz(l,:) Sz(l,size(Sz,2))]); Abs_p(p,:)=Abs(l,:);
E_abs_te(l,:)=(conj(E__te(1,:)+E__te(2,:)).*(E__te(1,:)+E__te(2,:)));
E_abs_tm(l,:)=(conj(E__tm(1,:)+E__tm(2,:)).*(E__tm(1,:)+E__tm(2,:)));
G_te(l,:)=real(nk(l,:)).*imag(nk(l,:)).*E_abs_te(l,:);
G_tm(l,:)=real(nk(l,:)).*imag(nk(l,:)).*E_abs_tm(l,:);
%----------------------------------------
%Solve diffusion eq (assume acceptor comes before donor material) — (from lab notebook p36)
t_d=1; t_a=1; %L_a=80e-10; L_d=200e-10; % donor acceptor diff. lengths and lifetimes, a-CuPc, d-C60
%Rand-Xue-Lange-Forrest and Peumans-Yak.-Forr.–ptcbi:30+-10, CuPc:100+-30; Stubinger–CuPc 68+-20
x_a=thickness(PV-1)/res; x_d=thickness(PV)/res;
exp_d=exp((Z((PV-1)*res)-Z((PV-1)*res+1:(PV)*res))/L_d);
exp_a=exp(-((Z((PV-1)*res)-Z((PV-2)*res:(PV-1)*res-1)))/L_a);
curr_d(l,:)=exp_d.*Abs(l,(PV-1)*res+1:(PV)*res);%.*diff(Z((PV-1)*res:(PV)*res));
curr_a(l,:)=exp_a.*Abs(l,(PV-2)*res+1:(PV-1)*res);%.*diff(Z((PV-2)*res:(PV-1)*res));
curr(l,:)=[curr_a(l,:) curr_d(l,:)];
EQE(p)=sum([sum(curr_a(l,:)) sum(curr_d(l,:))]);
```

```
%-----------------------------
PV_te(l,p)=Sz_te(PV-1,p)-Sz_te(PV,p); % absorption in the PV, normalized by incoming energy
PV_tm(l,p)=Sz_tm(PV-1,p)-Sz_tm(PV,p);
if abs(E_te(1,1)-E_te_l(1))>0.0001 or abs(E_te(2,1)-E_te_l(2))>0.0001
display('radiation condition failure TE')
end
if abs(E_tm(1,1)-E_tm_l(1))>0.0001 or abs(E_tm(2,1)-E_tm_l(2))>0.0001
display('radiation condition failure TM')
end
if p==80
aa=Sz_te;ba=Sz_tm;
end
R_te(l,p)=abs(E_te_l(2))^2; R_tm(l,p)=abs(E_tm_l(2))^2;
if isreal(i*kz(N))
T_te(l,p)=0; T_tm(l,p)=0;
else
T_te(l,p)=kz(N)/kz(1)*abs(E_te_r(1))^2;
T_tm(l,p)=epsilon(1)/epsilon(N)*kz(N)/kz(1)*abs(E_tm_r(1))^2;
end
end
end
Abs_te=1-(R_te+T_te); Abs_tm=1-(R_tm+T_tm);
% J_sc=EQE.*incoming_charge;
% eff = sum(norm_sun.*EQE)*abs_ratio*100 %do not multiply with dlambda since norm_sun is
already normalized
energy_array=h*light./wavelength_array/1e-9/q;
%figure(1),clf, plot(180/pi*theta_array,EQE*100./(1-R_tm)),title('IQE')
% dlmwrite('EQEoverR_theta.txt', [theta_array;EQE*100./(1-R_tm)]', 'delimiter', '\t', 'precision',
6)
%figure(2),clf, plot(180/pi*theta_array,EQE*100),title('EQE')
```

```
% dlmwrite('EQE_theta.txt', [theta_array;EQE*100]', 'delimiter', '\t', 'precision', 6)
%figure(3),clf, plot(theta_array*180/pi,R_tm','k'), title('Reflectivity')
% dlmwrite('R_theta.txt', [theta_array;R_tm]', 'delimiter', '\t', 'precision', 6)
%figure(4),clf, plot(theta_array*180/pi, (Sz_p(:,res)'-Sz_p(:,2*res)') + (Sz_p(:,2*res)'-Sz_p(:,3*res)')
,'r'), title('R')
%figure(4),clf, h=area(180/pi*theta_array,[(Sz_p(:,1)'-Sz_p(:,res)');(Sz_p(:,res)'-
Sz_p(:,2*res)');(Sz_p(:,2*res)'-Sz_p(:,3*res)');(Sz_p(:,3*res)'-Sz_p(:,4*res)')]');
% dlmwrite('Abs_theta.txt', [theta_array;(Sz_p(:,1)'-Sz_p(:,res)');(Sz_p(:,res)'-
Sz_p(:,2*res)');(Sz_p(:,2*res)'-Sz_p(:,3*res)');(Sz_p(:,3*res)'-Sz_p(:,4*res)')]', 'delimiter', '\t',
'precision', 6)
%title('Photocurrent');
%
plot(Z(101:299),20/19*Abs_p(2,101:299),Z(101:299),Abs_p(46,101:299)),legend('30','52'),title('Abs
vs Z'),xlabel('Z'),ylabel('Abs')
figure(1), clf, [x, y1, y2] = plotyy(theta_array*180/pi, EQE, theta_array*180/pi, R_tm', 'plot');
%title('Photocurrent and Reflectivity Angular Dependence');
%set(get(x(1),'Xlabel'),'String','incident angle (deg)');
%set(get(x(1),'Ylabel'),'String','photocurrent (EQE)', 'Color', 'r');
%set(get(x(2),'Ylabel'),'String','reflectivity');
%set(x(1),'XColor','k','YColor','k','ylimmode','auto','YTickMode','auto');
%set(x(2),'XColor','k','YColor','k','ylimmode','auto','YTickMode','auto');
%set(y1,'LineWidth',2,'Color','r');
%set(y2,'LineWidth',2,'Color','k');
figure(2),clf,surf(theta_array*180/pi,Z,E_tm_theta_z'),view(2),shading interp,
title('Tranverse Magnetic Electric Field Amplitude');
ylabel('Z');
xlabel('incident angle (deg)');
legend;
% plot(wavelength_array,EQE*100), title('EQE'), xlabel('wavelength (nm)'),ylabel('EQE (%)')
```

Appendix B

Numerical simulations for calculating the angular emission from an organic light emitting diode

This appendix presents a Matlab code that calculates the angular intensity emission profile of an organic light emitting diode, numerical data used in the chapter 'Integrated surface plasmon resonance biosensor based on organic semiconductor devices'. It assumes monochromatic emission of light of wavelength 650 nm, that coincided with the peak emission of the PtOEP dye complex used in the fabrication of the OLED. The dielectric layers are defined as a one dimensional stack of thickness t and dielectric constant ϵ. The dielectric constants of various organic and inorganic materials were calulated from the n and k values aquired with an Aquila nkd-8000 thin film measurement instrument. The code requires input of material files that contain n and k values for the 401-795 nm wavelength range. This simulation was adapted from work by Celebi et al.[5]

```
%note absorption of layer containing the exciton (’dipole layer’) must be zero
clf
clear
Planck=6.62e-34;
charge=1.6e-19;
light=3e8;
%radiative efficiency
q=1;
%free space lifetime - completely arbitrary scaling factor (1ns is typical
%for laser dyes
t0=1e-9;
% dielectric constant data first row is wavelength data (in nm) second row is dielectric constants
air = [200 1920; 1 1];
ITO = [200 250 300 350 400 450 500 550 600 650 700 750 800 850 900; 2.6000+i*2.8800
4.3500+i*3.0800 5.6700+i*1.4400 4.6176+i*0.3010 3.9996+i*0.0800 3.6099+i*0.0380
3.4224+i*0.0370 3.2399+i*0.0360 3.1683+i*0.0356 3.0624+i*0.0350 2.9928+i*0.0346
2.8899+i*0.0340 2.8222+i*0.0504 2.7554+i*0.0498 2.6567+i*0.0489];
gold = [317.897 326.263 335.081 344.389 354.229 364.647 375.697 387.438 399.935 413.267 427.517
442.786 459.185 476.846 495.92 516.583 539.044 563.545 652.526 688.778 729.294 774.875 826.533
885.571 953.692 1033.17; -0.2396 + 7.0067i -0.1999 + 6.8509i -0.2268 + 6.6886i -0.2890 + 6.5201i
-0.3875 + 6.4310i -0.5224 + 6.3904i -0.7564 + 6.4652i -0.9458 + 6.4817i -1.0770 + 6.4861i -1.1573
+ 6.4066i -1.1521 + 6.2701i -1.1854 + 5.9481i -1.3742 + 5.2648i -1.6831 + 4.4613i -2.5465 +
3.3709i -4.1247 + 2.5779i -6.2900 + 2.0422i -8.2008 + 1.7626i -9.8949 + 1.0458i -14.4144 + 1.2160i
-18.8956 + 1.4268i -23.5893 + 1.6913i -29.0168 + 2.0266i -34.5303 + 2.4696i -41.8052 + 3.0538i
-49.9109 + 3.8461i];
ag_nk=load(’ag.nk’); ag = [ag_nk(:,1)’; ag_nk(:,2)’.^2-ag_nk(:,3)’.^2+2*i*ag_nk(:,2)’.*ag_nk(:,3)’];
mg_nk=load(’Mg_palik.nk’); mg = [mg_nk(:,1)’;
mg_nk(:,2)’.^2-mg_nk(:,3)’.^2+2*i*mg_nk(:,2)’.*mg_nk(:,3)’];
bcp_nk=load(’bcp.nk’); bcp = [bcp_nk(:,1)’;
bcp_nk(:,2)’.^2-bcp_nk(:,3)’.^2+2*i*bcp_nk(:,2)’.*bcp_nk(:,3)’];
```

```
pedot_nk=load(’pedot.nk’); pedot = [pedot_nk(:,1)’;
pedot_nk(:,2)’.^2-pedot_nk(:,3)’.^2+2*i*pedot_nk(:,2)’.*pedot_nk(:,3)’];
alq3_nk =dlmread(’alq3_literature.dat’,’,’,0,0); alq3 = [0.1*alq3_nk(:,1)’;
alq3_nk(:,2)’.^2-alq3_nk(:,3)’.^2+2*i*alq3_nk(:,2)’.*alq3_nk(:,3)’];
test_glass=[200 1920; (1.72+i*0.0001)^2 (1.72+i*0.0001)^2];
glass_no_loss=[200 1920; 1.72^2 1.72^2];
tpd=bcp;
x_res=5e-4;
x_real=[-pi/2:x_res:-x_res]; % this is for the u=0 to u=1 region, it is negative so that u is
continuous from x_real to x_imag
x_imag=i*[x_res:x_res:1.8]; % this is the u>1 region change the upper bound to get more accurate
calculations of non-rad energy transfer very close to a metal
dx=[diff([x_real 0]) -diff([0 x_imag])];
x=[x_real x_imag]; u=cos(x);
size_u=max(size(u)); u_eq_1=max(size(x_real));
du=[diff(cos([x_real 0])) diff(cos([0 x_imag]))];
thickness_array=[1500e-10:500e-10:3000e-10];
wavelength=650; %in nanometers
for t=[1:max(size(thickness_array))],
% device structure
TPD_thickness=thickness_array(t);
TPD_thickness
thickness=[200e-10 1000e-10 400e-10 300e-10 TPD_thickness 200e-10 5000e-10];
%dipole position
dipole_layer=5;
dipole_position=00e-10; %distance from interface with previous layer)
epsilon(9)=interp1(glass_no_loss(1,:),glass_no_loss(2,:),wavelength);
epsilon(8)=interp1(glass_no_loss(1,:),glass_no_loss(2,:),wavelength);
epsilon(7)=interp1(ag(1,:),ag(2,:),wavelength);
epsilon(6)=interp1(tpd(1,:),tpd(2,:),wavelength);
```

```
epsilon(5)=interp1(alq3(1,:),alq3(2,:),wavelength);
epsilon(4)=interp1(bcp(1,:),bcp(2,:),wavelength);
epsilon(3)=interp1(mg(1,:),mg(2,:),wavelength);
epsilon(2)=interp1(ag(1,:),ag(2,:),wavelength);
epsilon(1)=interp1(air(1,:),air(2,:),wavelength);
N=max(size(epsilon));
k=2*pi/wavelength/1e-9*sqrt(epsilon);
u_crit=sqrt(1/epsilon(dipole_layer)); % total internal reflection
u_rad=max([1:max(size(u))].*(u_crit>u));
u_crit_glass=sqrt(epsilon(N-1)/epsilon(dipole_layer));
u_glass=max([1:max(size(u))].*(u_crit_glass>u));
z0=[0 cumsum(thickness)];
z0=z0-(z0(dipole_layer-1)+dipole_position); %set dipole position to z=0
% z0(8)=0
for n=[1:N],
h(n,:)=k(dipole_layer)*sqrt(epsilon(n)/epsilon(dipole_layer)-cos(x).^2);
end
% CB and FB are c'/c and f'/f respectively
CB(1,:)=0*x; %from radiation condition
FB(1,:)=0*x; %from radiation condition
for n=[2:dipole_layer],
R_perp(n,:)=(h(n,:)-h(n-1,:))./(h(n,:)+h(n-1,:));
R_para(n,:)=(epsilon(n)*h(n-1,:)-epsilon(n-1)*h(n,:))./(epsilon(n)*h(n-1,:)+epsilon(n-1)*h(n,:));
CB(n,:)=exp(-2*i*h(n,:)*z0(n-1)).*( R_perp(n,:)+CB(n-1,:).*exp(2*i*h(n-1,:)*z0(n-
1)))./(1+R_perp(n,:).*CB(n-1,:).*exp(2*i*h(n-1,:)*z0(n-1)));
FB(n,:)=exp(-2*i*h(n,:)*z0(n-1)).*(-R_para(n,:)+FB(n-1,:).*exp(2*i*h(n-1,:)*z0(n-1)))./(1-
R_para(n,:).*FB(n-1,:).*exp(2*i*h(n-1,:)*z0(n-1)));
end
% CT and FT are c/c' and f/f' respectively
CT(N,:)=0*x; %from radiation condition
```

```
FT(N,:)=0*x; %from radiation condition
for n=[N-1:-1:dipole_layer],
R_perp(n,:)=(h(n,:)-h(n+1,:))./(h(n,:)+h(n+1,:));
R_para(n,:)=(epsilon(n)*h(n+1,:)-
epsilon(n+1)*h(n,:))./(epsilon(n)*h(n+1,:)+epsilon(n+1)*h(n,:));
CT(n,:)=exp(2*i*h(n,:)*z0(n)).*( R_perp(n,:)+CT(n+1,:).*exp(-
2*i*h(n+1,:)*z0(n)))./(1+R_perp(n,:).*CT(n+1,:).*exp(-2*i*h(n+1,:)*z0(n)));
FT(n,:)=exp(2*i*h(n,:)*z0(n)).*(-R_para(n,:)+FT(n+1,:).*exp(-2*i*h(n+1,:)*z0(n)))./(1-
R_para(n,:).*FT(n+1,:).*exp(-2*i*h(n+1,:)*z0(n)));
end
c(dipole_layer,:)
=(CB(dipole_layer,:)+1).*CT(dipole_layer,:)./(1-CB(dipole_layer,:).*CT(dipole_layer,:));
cd(dipole_layer,:)=(CT(dipole_layer,:)+1).*CB(dipole_layer,:)./(1-
CB(dipole_layer,:).*CT(dipole_layer,:));
f_perp(dipole_layer,:) =
(FB(dipole_layer,:)+1).*FT(dipole_layer,:)./(1-FB(dipole_layer,:).*FT(dipole_layer,:));
fd_perp(dipole_layer,:)=
(FT(dipole_layer,:)+1).*FB(dipole_layer,:)./(1-FB(dipole_layer,:).*FT(dipole_layer,:));
f_para(dipole_layer,:)
=-(1-FB(dipole_layer,:)).*FT(dipole_layer,:)./(1-FB(dipole_layer,:).*FT(dipole_layer,:));
fd_para(dipole_layer,:)=
(1-FT(dipole_layer,:)).*FB(dipole_layer,:)./(1-FB(dipole_layer,:).*FT(dipole_layer,:));
for n=[dipole_layer:-1:2],
c(n-1,:) =0.5*exp( i*h(n-1,:)*z0(n-1)).*(((n==dipole_layer)+c(n,:)).*exp(-i*h(n,:)*z0(n-
1)).*(1+h(n,:)./h(n-1,:))+cd(n,:).*exp(i*h(n,:)*z0(n-1)).*(1-h(n,:)./h(n-1,:)));
cd(n-1,:)=0.5*exp(-i*h(n-1,:)*z0(n-1)).*(((n==dipole_layer)+c(n,:)).*exp(-i*h(n,:)*z0(n-1)).*(1-
h(n,:)./h(n-1,:))+cd(n,:).*exp(i*h(n,:)*z0(n-1)).*(1+h(n,:)./h(n-1,:)));
f_perp(n-1,:) =0.5*exp( i*h(n-1,:)*z0(n-1)).*(((n==dipole_layer)+f_perp(n,:)).*exp(-i*h(n,:)*z0(n-
1)).*(k(n)/k(n-1)+k(n-1)/k(n)*h(n,:)./h(n-1,:))+fd_perp(n,:).*exp(i*h(n,:)*z0(n-1)).*(k(n)/k(n-1)-
k(n-1)/k(n)*h(n,:)./h(n-1,:)));
```

```
fd_perp(n-1,:)=0.5*exp(-i*h(n-1,:)*z0(n-1)).*(((n==dipole_layer)+f_perp(n,:)).*exp(-i*h(n,:)*z0(n-
1)).*(k(n)/k(n-1)-k(n-1)/k(n)*h(n,:)./h(n-1,:))+fd_perp(n,:).*exp(i*h(n,:)*z0(n-1)).*(k(n)/k(n-
1)+k(n-1)/k(n)*h(n,:)./h(n-1,:)));

f_para(n-1,:) =0.5*exp( i*h(n-1,:)*z0(n-1)).*(((n==dipole_layer)+f_para(n,:)).*exp(-i*h(n,:)*z0(n-
1)).*(k(n)/k(n-1)+k(n-1)/k(n)*h(n,:)./h(n-1,:))+fd_para(n,:).*exp(i*h(n,:)*z0(n-1)).*(k(n)/k(n-1)-
k(n-1)/k(n)*h(n,:)./h(n-1,:)));

fd_para(n-1,:)=0.5*exp(-i*h(n-1,:)*z0(n-1)).*(((n==dipole_layer)+f_para(n,:)).*exp(-i*h(n,:)*z0(n-
1)).*(k(n)/k(n-1)-k(n-1)/k(n)*h(n,:)./h(n-1,:))+fd_para(n,:).*exp(i*h(n,:)*z0(n-1)).*(k(n)/k(n-
1)+k(n-1)/k(n)*h(n,:)./h(n-1,:)));

end

for n=[dipole_layer:N-1],

c(n+1,:) =0.5*exp( i*h(n+1,:)*z0(n)).*(c(n,:).*exp(-
i*h(n,:)*z0(n)).*(1+h(n,:)./h(n+1,:))+((n==dipole_layer)+cd(n,:)).*exp(i*h(n,:)*z0(n)).*(1-
h(n,:)./h(n+1,:)));

cd(n+1,:)=0.5*exp(-i*h(n+1,:)*z0(n)).*(c(n,:).*exp(-i*h(n,:)*z0(n)).*(1-
h(n,:)./h(n+1,:))+((n==dipole_layer)+cd(n,:)).*exp(i*h(n,:)*z0(n)).*(1+h(n,:)./h(n+1,:)));

f_perp(n+1,:) =0.5*exp( i*h(n+1,:)*z0(n)).*(f_perp(n,:).*exp(-
i*h(n,:)*z0(n)).*(k(n)/k(n+1)+k(n+1)/k(n)*h(n,:)./h(n+1,:))+(fd_perp(n,:)+(n==dipole_layer)).*exp(i*h(n,:)*z0(n)).*(k(
k(n+1)/k(n)*h(n,:)./h(n+1,:)));

fd_perp(n+1,:)=0.5*exp(-i*h(n+1,:)*z0(n)).*(f_perp(n,:).*exp(-i*h(n,:)*z0(n)).*(k(n)/k(n+1)-
k(n+1)/k(n)*h(n,:)./h(n+1,:))+(fd_perp(n,:)+(n==dipole_layer)).*exp(i*h(n,:)*z0(n)).*(k(n)/k(n+1)+k(n+1)/k(n)*h(n,:)

f_para(n+1,:) =0.5*exp( i*h(n+1,:)*z0(n)).*(f_para(n,:).*exp(-
i*h(n,:)*z0(n)).*(k(n)/k(n+1)+k(n+1)/k(n)*h(n,:)./h(n+1,:))+(fd_para(n,:)-
(n==dipole_layer)).*exp(i*h(n,:)*z0(n)).*(k(n)/k(n+1)-k(n+1)/k(n)*h(n,:)./h(n+1,:)));

fd_para(n+1,:)=0.5*exp(-i*h(n+1,:)*z0(n)).*(f_para(n,:).*exp(-i*h(n,:)*z0(n)).*(k(n)/k(n+1)-
k(n+1)/k(n)*h(n,:)./h(n+1,:))+(fd_para(n,:)-
(n==dipole_layer)).*exp(i*h(n,:)*z0(n)).*(k(n)/k(n+1)+k(n+1)/k(n)*h(n,:)./h(n+1,:)));

end

b_perp(t,:) = real(dx.*(3/2*(f_perp(dipole_layer,:)+fd_perp(dipole_layer,:)).*(cos(x).^3)));
```

```
b_para(t,:) =
real(dx.*(3/4*((c(dipole_layer,:)+cd(dipole_layer,:))+(sin(x).^2).*(f_para(dipole_layer,:)-
fd_para(dipole_layer,:))).*cos(x)));


b_perp_sum(t) = 1-q + q*(1+sum(b_perp(t,:)));
b_para_sum(t) = 1-q + q*(1+sum(b_para(t,:)));
for n=[1:N-1],
power_perp_u(t,:,n) = (real(du.*(-3/4*q*(u.^3)./abs(1-u.^2).*sqrt(epsilon(n)/epsilon(dipole_layer)-
u.^2).*conj(sqrt(epsilon(n)))/sqrt(epsilon(n)).*(f_perp(n,:).*exp(-i*h(n,:)*z0(n))-
(fd_perp(n,:)+(n==dipole_layer)).*exp(i*h(n,:)*z0(n))).*conj((f_perp(n,:).*exp(-
i*h(n,:)*z0(n))+(fd_perp(n,:)+(n==dipole_layer)).*exp(i*h(n,:)*z0(n)))))));
power_para_u(t,:,n) =
(real(du.*(-3/8*q*u.*(conj(sqrt(epsilon(n)/epsilon(dipole_layer)-u.^2))./abs(1-u.^2).*(c(n,:).*exp(-
i*h(n,:)*z0(n))+(cd(n,:)+(n==dipole_layer)).*exp(i*h(n,:)*z0(n))).*conj((c(n,:).*exp(-
i*h(n,:)*z0(n))-
(cd(n,:)+(n==dipole_layer)).*exp(i*h(n,:)*z0(n))))+sqrt(epsilon(n)/epsilon(dipole_layer)-
u.^2).*conj(sqrt(epsilon(n)))/sqrt(epsilon(n)).*(f_para(n,:).*exp(-i*h(n,:)*z0(n))-(fd_para(n,:)-
(n==dipole_layer)).*exp(i*h(n,:)*z0(n))).*conj((f_para(n,:).*exp(-i*h(n,:)*z0(n))+(fd_para(n,:)-
(n==dipole_layer)).*exp(i*h(n,:)*z0(n))))))));
end
power_perp=sum(power_perp_u,2); power_para=sum(power_para_u,2);
frac_perp(t,:)=diff([0 power_perp(t,:) 0]);
frac_para(t,:)=diff([0 power_para(t,:) 0]);
rad_perp=sum(power_perp_u(:,[1:u_rad],N-1),2);
rad_para=sum(power_para_u(:,[1:u_rad],N-1),2);
end
outcoupling=2/3*rad_para'./b_para_sum+1/3*rad_perp'./b_perp_sum;
b_total_sum=2/3*b_para_sum+1/3*b_perp_sum;
frac_total=2/3*frac_para+1/3*frac_perp;
glass=((abs(frac_total(:,N))+abs(frac_total(:,N-1)))'./b_total_sum)-outcoupling;
```

```
hold off
% figure(1),clf
%
area(1e9*dipole_position_array,[abs(frac_perp(:,2)’./b_perp_sum);abs(frac_perp(:,3)’./b_perp_sum);
abs(frac_perp(:,4)’./b_perp_sum);abs(frac_perp(:,6)’./b_perp_sum);abs(frac_perp(:,7)’./b_perp_sum);abs(frac_perp(:,8)’./b_pe
% title(’Perpendicular Dipole energy Transfer’),xlabel(’Dipole distance to HTL (nm)’),
ylabel(’Coupling efficiency’), legend(’ag’,’mg’,’bcp’,’tpd’,’pedot’,’ITO’,’glass’,’AIR’)
% hold on,
% plot(1e9*dipole_position_array,1-rad_perp’./b_perp_sum)
% hold off
% %
% figure(2),clf
%
area(1e9*dipole_position_array,[abs(frac_para(:,2)’./b_para_sum);abs(frac_para(:,3)’./b_para_sum);
abs(frac_para(:,4)’./b_para_sum);abs(frac_para(:,6)’./b_para_sum);abs(frac_para(:,7)’./b_para_sum);abs(frac_para(:,8)’./b_pa
% title(’Parallel Dipole energy Transfer’),xlabel(’Dipole distance to HTL (nm)’), ylabel(’Coupling
efficiency’), legend(’ag’,’mg’,’bcp’,’tpd’,’pedot’,’ITO’,’glass’,’AIR’)
% hold on,
% plot(1e9*dipole_position_array,1-rad_para’./b_para_sum)
% hold off
% % %
figure(1),clf
area(1e9*thickness_array,[outcoupling; glass;
abs(frac_total(:,7)’./b_total_sum);abs(frac_total(:,6)’./b_total_sum)+abs(frac_total(:,4)’./b_total_sum);abs(frac_total(:,3)’./b_
xlabel(’TPD thickness (nm)’), ylabel(’Coupling efficiency’), legend(’air’,’glass’,’Bottom
Ag’,’Organics’,’Top Ag’)
figure(4),clf
theta_air=real(acos(sqrt(1-epsilon(dipole_layer)*u([2:u_rad]).ˆ2))); % Remember k_0 is defined at
dipole layer
theta_glass=real(acos(sqrt(1-epsilon(dipole_layer)/epsilon(N)*u([2:u_glass]).ˆ2)));
```

```
for t=[1:max(size(thickness_array))],
p_angle_air=(power_perp_u(t,[2:u_rad],N-1).*sqrt(1/epsilon(dipole_layer))./tan(theta_air));
% polar(theta_air,p_angle_air/max(p_angle_air),’r-’),hold
on,polar(-theta_air,p_angle_air/max(p_angle_air),’r-’)
p_angle_glass=(power_perp_u(t,[2:u_glass],N-
1).*sqrt(epsilon(N)/epsilon(dipole_layer))./tan(theta_glass));
polar(theta_glass,p_angle_glass/max(p_angle_glass),’b-’),hold
on,polar(-theta_glass,p_angle_glass/max(p_angle_glass),’b-’)
end
%polar(theta_air,cos(theta_air),’g-’),polar(-theta_air,cos(theta_air),’g-’),
title(’Perpendicular dipole angular emission profile in glass (blue) and air (red) compared to ideal
(green)’)
hold off
figure(5),clf
theta_air=real(acos(sqrt(1-epsilon(dipole_layer)*u([2:u_rad]).^2))); % Remember k_0 is defined at
dipole layer
theta_glass=real(acos(sqrt(1-epsilon(dipole_layer)/epsilon(N)*u([2:u_glass]).^2)));
for t=[1:max(size(thickness_array))],
p_angle_air=(power_para_u(t,[2:u_rad],N-1).*sqrt(1/epsilon(dipole_layer))./tan(theta_air));
% polar(theta_air,p_angle_air/max(p_angle_air),’r-’),hold
on,polar(-theta_air,p_angle_air/max(p_angle_air),’r-’)
p_angle_glass=(power_para_u(t,[2:u_glass],N-
1).*sqrt(epsilon(N)/epsilon(dipole_layer))./tan(theta_glass));
polar(theta_glass,p_angle_glass/max(p_angle_glass),’b-’),hold
on,polar(-theta_glass,p_angle_glass/max(p_angle_glass),’b-’)
end
%polar(theta_air,cos(theta_air),’g-’),polar(-theta_air,cos(theta_air),’g-’),
title(’Parallel dipole angular emission profile in glass (blue) and air (red) compared to ideal
(green)’)
hold off
```

```
figure(6),clf
theta_air=real(acos(sqrt(1-epsilon(dipole_layer)*u([2:u_rad]).^2))); % Remember k_0 is defined at
dipole layer
theta_glass=real(acos(sqrt(1-epsilon(dipole_layer)/epsilon(N)*u([2:u_glass]).^2)));
for t=[1:max(size(thickness_array))],
p_angle_air=2/3*(power_para_u(t,[2:u_rad],N-
1).*sqrt(1/epsilon(dipole_layer))./tan(theta_air))+1/3*(power_perp_u(t,[2:u_rad],N-
1).*sqrt(1/epsilon(dipole_layer))./tan(theta_air));
% polar(theta_air,p_angle_air/max(p_angle_air),'r-'),hold
on,polar(-theta_air,p_angle_air/max(p_angle_air),'r-')
p_angle_glass=2/3*(power_para_u(t,[2:u_glass],N-
1).*sqrt(epsilon(N)/epsilon(dipole_layer))./tan(theta_glass))+1/3*(power_perp_u(t,[2:u_glass],N-
1).*sqrt(epsilon(N)/epsilon(dipole_layer))./tan(theta_glass));
polar(theta_glass,p_angle_glass/max(p_angle_glass),'b-'),hold
on,polar(-theta_glass,p_angle_glass/max(p_angle_glass),'b-'),hold on
%pause
end
%polar(theta_air,cos(theta_air),'g-'),polar(-theta_air,cos(theta_air),'g-'),
title('Average angular emission profile in glass (blue) and air (red) compared to ideal (green)')
hold off
%plot(power_para_u(t,[2:u_glass],N-1)),hold on, plot(power_para_u(t,[2:u_rad],N-1),'r')
%sum(diff([0 theta_air]).*p_angle_air.*sin(theta_air)./diff(u([1:u_rad])))./b_para_sum(t)
%sum(diff([0
%theta_glass]).*p_angle_glass.*sin(theta_glass)./diff(u([1:u_glass])))./b_para_sum(t)
```

Bibliography

[1] Jung, LS, Campbell, CT, Chinowsky, TM, Mar, MN, Yee, SS (1998) Quantitative interpretation of the response of surface plasmon resonance sensors to adsorbed films. *Langmuir* 14:5636-5648.

[2] Homola, J, Yee, SS, Gauglitz, G (1999) Surface plasmon resonance sensors: review. *Sensors and Actuators B-Chemical* 54:3-15.

[3] Rich, RL, Myszka, DG (2007) Survey of the year 2006 commercial optical biosensor literature. *Journal of Molecular Recognition* 20:300-366.

[4] Mapel, JK, Singh, M, Celebi, K and M. A. Baldo (2007) Plasmonic excitation of organic double heterostructure solar cells. *Applied Physics Letters* 90:121102-121105.

[5] Celebi, K, Heidel, TD, Baldo, MA (2007) Simplified calculation of dipole energy transport in a multilayer stack using dyadic green's functions. *Optics Express* 15:1762-1772.

[6] C. L. Mulder and K. Celebi and K. M. Milaninia and M. A. Baldo (2007) Saturated and efficient blue phosphorescent organic light emitting devices with Lambertian angular emission. *Applied Physics Letters* 90:211109-211112.

[7] Iga, K. (2000) Surface-emitting laser-its birth and generation of new optoelectronics field. *Selected Topics in Quantum Electronics, IEEE Journal of* 6:1201-1215.

[8] B. Johnsson, S. Lofas, G. Lindquist (1991) Immobilization of proteins to a carboxymethyldextran-modified gold surface for biospecific interaction analysis in surface plasmon resonance sensors. *Analytical Biochemistry* 198:268-277.

[9] Zhang, S et al. (2007) Surface plasmon resonance characterization of thermally evaporated thin gold films. *Surface Science* 601:5445-5458.

[10] Castellana, ET, Kataoka, S, Albertorio, F, Cremer, PS (2006) Direct writing of metal nanoparticle films inside sealed microfluidic channels. *Analytical Chemistry* 78:107-112.

[11] Harder, P, Grunze, M, Dahint, R, Whitesides, GM, Laibinis, PE (1998) Molecular conformation in oligo(ethylene glycol)-terminated self-assembled monolayers on gold and silver surfaces determines their ability to resist protein adsorption. *Journal of Physical Chemistry B* 102:426-436.

[12] Ostuni, E, Chapman, RG, Holmlin, RE, Takayama, S, Whitesides, GM (2001) A survey of structure-property relationships of surfaces that resist the adsorption of protein. *Langmuir* 17:5605-5620

[13] Lofas, S, Johnsson, B (1990) A novel hydrogel matrix on gold surfaces in surface-plasmon resonance sensors for fast and efficient covalent immobilization of ligands. *Journal of the Chemical Society-Chemical Communications* 21:1526-1528.

[14] Akkoyun, A, Bilitewski, U (2002) Optimisation of glass surfaces for optical immunosensors. *Biosensors and Bioelectronics* 17:655-664.

[15] Potscavage, W. J., Yoo, S., Domercq, B., Kippelen, B (2007) Encapsulation of pentacene/C_{60} organic solar cells with Al_2O_3 deposited by atomic layer deposition. *Applied Physics Letters* 90:253511-253514.

[16] Hamed, A., Sun, Y. Y., Tao, Y. K., Meng, R. L., Hor, P. H., (1993) Effects of oxygen and illumination on the in situ conductivity of $C60$ thin films. *Physical Review B* 47:10873-10880.

[17] Forrest, SR (1997) Ultrathin Organic Films Grown by Organic Molecular Beam Deposition and Related Techniques. *Chemical Reviews* 97:1793-1896.

[18] AK Abass, A Krier, and RA Collins. The influence of chlorine on the electrical properties of lead phthalocyanine thin-film gas sensors. *Journal of Physics D-Applied Physics*, 26(7):1120–1124, JUL 14 1993.

[19] A Altindal, ZZ Ozturk, S Dabak, and O Bekaroglu. Halogen sensing using thin films of crosswise-substituted phthalocyanines. *Sensors and Actuators B-Chemical*, 77(1-2):389–394, JUN 15 2001.

[20] M Bouvet, G Guillaud, A Leroy, A Maillard, S Spirkovitch, and FG Tournilhac. Phthalocyanine-based field-effect transistor as ozone sensor. *Sensors and Actuators B-Chemical*, 73(1):63–70, FEB 25 2001.

[21] M Bouvet, A Leroy, J Simon, F Tournilhac, G Guillaud, P Lessnick, A Maillard, S Spirkovitch, M Debliquy, A de Haan, and A Decroly. Detection and titration of ozone using metallophthalocyanine based field effect transistors. *Sensors and Actuators B-Chemical*, 72(1):86–93, JAN 5 2001.

[22] TM Chinowsky, JG Quinn, DU Bartholomew, R Kaiser, and JL Elkind. Performance of the Spreeta 2000 integrated surface plasmon resonance affinity sensor. *Sensors and Actuators B-Chemical*, 91(1-3):266–274, JUN 1 2003.

[23] B Crone, A Dodabalapur, A Gelperin, L Torsi, HE Katz, AJ Lovinger, and Z Bao. Electronic sensing of vapors with organic transistors. *Applied Physics Letters*, 78(15):2229–2231, APR 9 2001.

[24] A Diez, MV Andres, and JL Cruz. In-line fiber-optic sensors based on the excitation of surface plasma modes in metal-coated tapered fibers. *Sensors and Actuators B-Chemical*, 73(2-3):95–99, MAR 10 2001.

[25] J Dostalek, J Ctyroky, J Homola, E Brynda, M Skalsky, P Nekvindova, J Spirkova, J Skvor, and J Schrofel. Surface plasmon resonance biosensor based

on integrated optical waveguide. *Sensors and Actuators B-Chemical*, 76(1-3):8–12, JUN 1 2001.

[26] J Dostalek, J Homola, and M Miler. Rich information format surface plasmon resonance biosensor based on array of diffraction gratings. *Sensors and Actuators B-Chemical*, 107(1):154–161, MAY 27 2005.

[27] DJ Gundlach, TN Jackson, DG Schlom, and SF Nelson. Solvent-induced phase transition in thermally evaporated pentacene films. *Applied Physics Letters*, 74(22):3302–3304, MAY 31 1999.

[28] RD Harris, BJ Luff, JS Wilkinson, J Piehler, A Brecht, G Gauglitz, and RA Abuknesha. Integrated optical surface plasmon resonance immunoprobe for simazine detection. *Biosensors & Bioelectronics*, 14(4):377–386, APR 30 1999.

[29] RD Harris and JS Wilkinson. Wave-guide Surface plasmon resonance sensors. *Sensors and Actuators B-Chemical*, 29(1-3):261–267, OCT 1995.

[30] J Homola. Optical fiber sensor based on surface plasmon excitation. *Sensors and Actuators B-Chemical*, 29(1-3):401–405, OCT 1995.

[31] J Homola, HBB Lu, GG Nenninger, J Dostalek, and SS Yee. A novel multichannel surface plasmon resonance biosensor. *Sensors and Actuators B-Chemical*, 76(1-3):403–410, JUN 1 2001.

[32] N Imanaka and I Hasegawa. Nitrogen monoxide gas sensor operating at intermediate temperature region. *Sensor Letters*, 1(1):51–55, DEC 2003.

[33] D James, SM Scott, Z Ali, and WT O'Hare. Chemical sensors for electronic nose systems. *Microchimica Acta*, 149(1-2):1–17, FEB 2005.

[34] RC Jorgenson and SS Yee. Control of the dynamic range and sensitivity of a surface plasmon resonance based fiber optic sensor. *Sensors and Actuators B-Physical*, 43(1-3):44–48, MAY 1994.

[35] AV Kabashin and PI Nikitin. Surface plasmon resonance interferometer for bio- and chemical-sensors. *Optics Communications*, 150(1-6):5–8, MAY 1 1998.

[36] H Kano and S Kawata. Surface plasmon sensor for absorption sensitivity enhancement. *Applied Optics*, 33(22):5166–5170, AUG 1 1994.

[37] NS Lebedeva, EV Trofimova, NA Pavlycheva, and AI Vyugin. Molecular complexes of phthalocyanine with organic solvents. *Russian Journal of Organic Chemistry*, 38(8):1195–1199, AUG 2002.

[38] YL Lee, CY Sheu, and RH Hsiao. Gas sensing characteristics of copper phthalocyanine films: effects of film thickness and sensing temperature. *Sensors and Actuators B-Chemical*, 99(2-3):281–287, MAY 1 2004.

[39] YL Lee, WC Tsai, CH Chang, and YM Yang. Effects of heat annealing on the film characteristics and gas sensing properties of substituted and un-substituted copper phthalocyanine films. *Applied Surface Science*, 172(3-4):191–199, MAR 15 2001.

[40] YL Lee, WC Tsai, and JR Maa. Effects of substrate temperature on the film characteristics and gas-sensing properties of copper phthalocyanine films. *Applied Surface Science*, 173(3-4):352–361, MAR 29 2001.

[41] F Liao, C Chen, and V Subramanian. Organic TFTs as gas sensors for electronic nose applications. *Sensors and Actuators B-Chemical*, 107(2):849–855, JUN 29 2005.

[42] CJ Liu, JJ Shih, and YH Ju. Surface morphology and gas sensing of nickel phthalocyanine thin characteristics films. *Sensors and Actuators B-Chemical*, 99(2-3):344–349, MAY 1 2004.

[43] K Matsubara, S Kawata, and S Minami. A compact surface plasmon resonance sensor for measurement of water in process. *Applied Spectroscopy*, 42(8):1375–1379, NOV-DEC 1988.

[44] AD McFarland and RP Van Duyne. Single silver nanoparticles as real-time optical sensors with zeptomole sensitivity. *Nano Letters*, 3(8):1057–1062, AUG 2003.

[45] J Melendez, R Carr, DU Bartholomew, K Kukanskis, J Elkind, S Yee, C Furlong, and R Woodbury. A commercial solution for surface plasmon sensing. *Sensors and Actuators B-Chemical*, 35(1-3):212–216, SEP 1996.

[46] F Meriaudeau, T Downey, A Wig, A Passian, M Buncick, and TL Ferrell. Fiber optic sensor based on gold island plasmon resonance. *Sensors and Actuators B-Chemical*, 54(1-2):106–117, JAN 25 1999.

[47] KA Miller, RD Yang, MJ Hale, J Park, B Fruhberger, CN Colesniuc, IK Schuller, AC Kummel, and WC Trogler. Electrode independent chemoresistive response for cobalt phthalocyanine in the space charge limited conductivity regime. *Journal of Physical Chemistry B*, 110(1):361–366, JAN 12 2006.

[48] K Mitsui, Y Handa, and K Kajikawa. Optical fiber affinity biosensor based on localized surface plasmon resonance. *Applied Physics Letters*, 85(18):4231–4233, NOV 1 2004.

[49] T Miyata and T Minami. Chlorine gas sensors with high sensitivity using Mg-phthalocyanine thin films. *Applied Surface Science*, 244(1-4):563–567, MAY 15 2005.

[50] JJ Mock, DR Smith, and S Schultz. Local refractive index dependence of plasmon resonance spectra from individual nanoparticles. *Nano Letters*, 3(4):485–491, APR 2003.

[51] SG Nelson, KS Johnston, and SS Yee. High sensitivity surface plasmon resonance sensor based on phase detection. *Sensors and Actuators B-Chemical*, 35(1-3):187–191, SEP 1996.

[52] GG Nenninger, M Piliarik, and J Homola. Data analysis for optical sensors based on spectroscopy of surface plasmons. *Measurement Science & Technology*, 13(12):2038–2046, DEC 2002.

[53] GG Nenninger, P Tobiska, J Homola, and SS Yee. Long-range surface plasmons for high-resolution surface plasmon resonance sensors. *Sensors and Actuators B-Chemical*, 74(1-3):145–151, APR 15 2001.

[54] MS Nieuwenhuizen, AJ Nederlof, and AW Barendsz. Metallophthalocyanines as chemical intefaces on a surface acoustic wave gas sensor for nitrogen dioxide. *Analytical Chemistry*, 60(3):230–235, FEB 1 1988.

[55] PI Nikitin, AN Grigorenko, AA Beloglazov, MV Valeiko, AI Savchuk, OA Savchuk, G Steiner, C Kuhne, A Huebner, and R Salzer. Surface plasmon resonance interferometry for micro-array biosensing. *Sensors and Actuators A-Physical*, 85(1-3):189–193, AUG 25 2000.

[56] NA Rakow and KS Suslick. A colorimetric sensor array for odour visualization. *Nature*, 406(6797):710–713, AUG 17 2000.

[57] R Rella, J Spadavecchia, G Ciccarella, P Siciliano, G Vasapollo, and L Valli. Optochemical vapour detection using spin coated thin films of metal substituted phthalocyanines. *Sensors and Actuators B-Chemical*, 89(1-2):86–91, MAR 1 2003.

[58] A Rosa and EJ Baerends. Origin and relevance of the staggering in one dimensional molecular metals - a density functional study of metallophthalocyanine model dimers. *Inorganic Chemistry*, 31(23):4717–4726, NOV 11 1992.

[59] J Sen and KS Suslick. Shape-selective discrimination of small organic molecules. *Journal of the American Chemical Society*, 122(46):11565–11566, NOV 22 2000.

[60] SA Shen, T Liu, and JH Guo. Optical phase-shift detection of surface plasmon resonance. *Applied Optics*, 37(10):1747–1751, APR 1 1998.

[61] R Slavik, J Homola, and J Ctyroky. Single-mode optical fiber surface plasmon resonance sensor. *Sensors and Actuators B-Chemical*, 54(1-2):74–79, JAN 25 1999.

[62] R Slavik, J Homola, J Ctyroky, and E Brynda. Novel spectral fiber optic sensor based on surface plasmon resonance. *Sensors and Actuators B-Chemical*, 74(1-3):106–111, APR 15 2001.

[63] J Spadavecchia, G Ciccarella, and R Rella. Optical characterization and analysis of the gas/surface adsorption phenomena on phthalocyanines thin films for gas sensing application. *Sensors and Actuators B-Chemical*, 106(1):212–220, APR 29 2005.

[64] J Spadavecchia, G Ciccarella, P Siciliano, S Capone, and R Rella. Spin-coated thin films of metal porphyrin-phthalocyanine blend for an optochemical sensor of alcohol vapours. *Sensors and Actuators B-Chemical*, 100(1-2):88–93, JUN 1 2004.

[65] J Spadavecchia, G Ciccarella, L Valli, and R Rella. A novel multisensing optical approach based on a single phthalocyanine thin films to monitoring volatile organic compounds. *Sensors and Actuators B-Chemical*, 113(1):516–525, JAN 17 2006.

[66] J Spadavecchia, G Ciccarella, G Vasapollo, P Siciliano, and R Rella. UV-Vis absorption optosensing materials based on metallophthalocyanines thin films. *Sensors and Actuators B-Chemical*, 100(1-2):135–138, JUN 1 2004.

[67] O Tal, Y Rosenwaks, Y Preezant, N Tessler, CK Chan, and A Kahn. Direct determination of the hole density of states in undoped and doped amorphous organic films with high lateral resolution. *Physical Review Letters*, 95(25), DEC 16 2005.

[68] L Torsi, A Dodabalapur, L Sabbatini, and PG Zambonin. Multi-parameter gas sensors based on organic thin-film-transistors. *Sensors and Actuators B-Chemical*, 67(3):312–316, SEP 1 2000.

[69] MCJM Vissenberg and M Matters. Theory of the field-effect mobility in amorphous organic transistors. *Physical Review B*, 57(20):12964–12967, MAY 15 1998.

[70] JY Wang, ZA Luthey-Schulten, and KS Suslick. Is the olfactory receptor a metalloprotein? *Proceedings of the National Academy of Scieces of the United States of America*, 100(6):3035–3039, MAR 18 2003.

[71] AW Wark, HJ Lee, and RM Corn. Long-range surface plasmon resonance imaging for bioaffinity sensors. *Analytical Chemistry*, 77(13):3904–3907, JUL 1 2005.

[72] D Wohrle. Phthalocyanines in macromolecular phases - Methods of synthesis and properties of the materials. *Macromolecular Rapid Communications*, 22(2):68–97, FEB 8 2001.

[73] SY Wu, HP Ho, WC Law, CL Lin, and SK Kong. Highly sensitive differential phase-sensitive surface plasmon resonance biosensor based on the Mach-Zehnder configuration. *Optics Letters*, 29(20):2378–2380, OCT 15 2004.